Magnetohydrodynamic Modeling of Convection inside Electromagnetically-Levitated Molten $Fe_{50}Co_{50}$ Droplets

Submitted By
Xiao Xiao

IN PARTIAL FULFILLMENT OF THE REQUIREMENTS FOR THE DEGREE OF

MASTER OF SCIENCE IN MECHANICAL ENGINEERING

School of Engineering
Tufts University
Medford, Massachusetts

May 2013

Signature of Author:
Xiao Xiao

Certified By:
Associate Professor Douglas M. Matson
Department of Mechanical Engineering
Tufts University

Committee:
Assistant Professor Luisa Chiesa
Department of Mechanical Engineering
Tufts University

Committee:
Professor Robert W. Hyers
Dept. of Mechanical and Industrial Engineering
University of Massachusetts - Amherst

Abstract

A magnetohydrodynamic model is developed to predict the convection velocity inside electromagnetically-levitated molten alloy droplets utilizing a commercial computational fluid dynamics package. The internal convection velocity of levitated molten $Fe_{50}Co_{50}$ droplet is simulated versus testing temperature, sample undercooling, coil current and control voltage in electromagnetic levitation experiments in support of future microgravity materials experiments on board the International Space Station. The range of internal convection velocity for the levitated molten samples is evaluated and used to define the accessible Reynolds number to identify the laminar-turbulent transition behavior for these experiments.

Acknowledgements

I would like to thank my advisor Professor Douglas Matson who advises, supports, and encourages me all the time. In the period of my study, research, and thesis writing, Prof. Matson always leads me to the right direction and makes detailed suggestions patiently in many aspects.

I would like to address special thanks to Dr. Jonghyun Lee, who teaches and advises me with great patience during the whole period of my research. I would like to thank Professor Robert Hyers of Umass-Amherst, who always gives very valuable suggestions. I would like to thank all the professors and staffs who taught and helped with me in department of mechanical engineering at Tufts. I would like to thank NASA for their funding support under grants NNX08AL21G and NNX10AV27G.

Finally, I would like to thank my family for their support through my life.

Table of Contents

List of Tables

List of Figures

1 Introduction

The objective of this thesis is to predict convection velocity inside electromagnetically-levitated (EML) molten $Fe_{50}Co_{50}$ droplets versus a series of testing parameters, and define the limits to convection accessible during EML testing, in support of the microgravity materials experiments in International Space Station (ISS).

Iron-cobalt is an industrially very important alloy, and the alloy's mechanical and thermophysical property is related to its microstructure. Previous research [1] showed that during the solidification process, the internal convection flow of the molten alloy significantly influences the solidified alloy's microstructure. For undercooled molten alloys, they would experience double recalescence, a two-steps solidification process, forming the metastable ferrite phase first and then transforming to the stable austenite phase. During this period, the patterns and timing of nucleation events and dendrites growth is important in solidified alloys' microstructures and physical properties. If the metastable phase stays for a longer time, more body-centered cubic crystal structures would be maintained, and not overwhelmed by growing dendrites in the stable phase, which would result in finer microstructures that may lead to better material and mechanical properties. The effects of internal convection on the lifetime of metastable phase have been presented in [1] and [2]. The convection with certain velocity would cause the alloy's primary dendrites to bend and the secondary dendrites touch with each other, triggering the nucleation of the undercooled samples.

To investigate the solidification process of molten alloy, levitation technique is utilized. Electromagnetic levitation is an effective containerless processing technique for solidification research of metals and alloys, as well as a tool used to measure their thermophysical properties. In electromagnetic levitation experiments, the molten samples can be processed and measured through a wide range of temperatures, achieving deep undercooling which traditional contacting processing methods cannot deal with. When the sample is levitated, the electromagnetic force induced by alternating current through the coils will support the sample against gravity and heat it simultaneously. The levitated alloy sample will be melted and form a liquid droplet, and the electromagnetic field will generate driving force inside the droplet, introducing internal stirrings and recirculations of the molten alloy droplet.

We are interested in predicting the internal convection velocity in real electromagnetic levitation experiments, so that we could have further study on the solidification process of the alloys. However, the samples are opaque and highly reactive in high temperature and large electromagnetic field therefore it is hard to use conventional techniques to measure the convection flow directly inside the droplets [3]. Thus, we utilize numerical simulation to investigate the internal convection velocities and their limits as functions of testing temperatures, control voltage and current in actual electromagnetically levitation experiments.

2 Background

2.1 Containerless Processing Techniques

Containerless processing techniques are powerful in material research including evaluation of material properties, investigation of metastable phases, and control of phase selection. It has application to metals, various alloys, and semiconductors. In the containerless processing facility, the sample is levitated and avoids reacting with crucibles and containment vessels. It brings several benefits that traditional processing does not have, such as reduction of contamination at high temperature, access to metastable phases and the undercooled liquid is accessible, and precise evaluation of material properties due to access to the free surface of the sample.

There are several levitation approaches in containerless processing, such as electrostatic levitation (ESL), electromagnetic levitation (EML), aerodynamic levitation, and acoustic levitation, etc. Compared to other levitation approaches, EML and ESL have better stabilization of the levitated sample, and the material could be processed in vacuum environment, so that they are very appropriate for thermophysical property measurement, and research in undercooling and solidification process of metals and alloys.

In EML (Figure 1), the sample is placed inside a set of coils with an imposed high frequency current, eddy currents will be induced on the sample's surface, and electromagnetic body forces will position the sample such that it will be heated and melt by Joule heating. The EML facility contains electromagnetic levitation coils that

have positioning and heating circuit, nucleation trigger, pyrometer, and video system that records the status of the sample in real-time. Based on the temperature-time profile from the pyrometer, and sample's real-time status from the video, we could determine the material's thermophysical properties, such as density, viscosity, and solidification velocity, etc. Such EML facility could be set up either on ground or in the space.

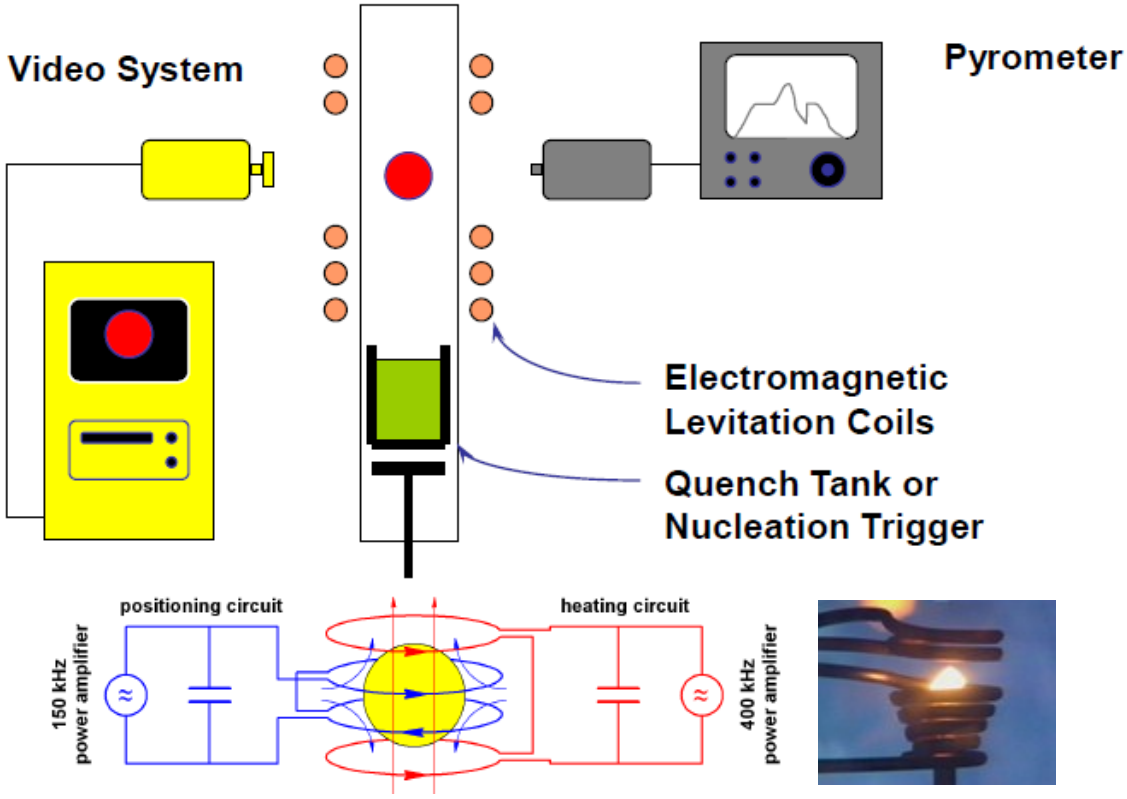

Figure 1: Electromagnetic Levitation (EML)

In ESL (Figure 2), the sample is placed between a set of opposite electrode, and the charged sample is supported by the electric field. A laser source is utilized to heat the sample, and another laser is set to track the sample with a controller that keeps the sample stable. Similarly, there is pyrometer and video system in ESL facility. ESL is

currently only utilized on ground but a space system is under development by the Japanese space agency JAXA.

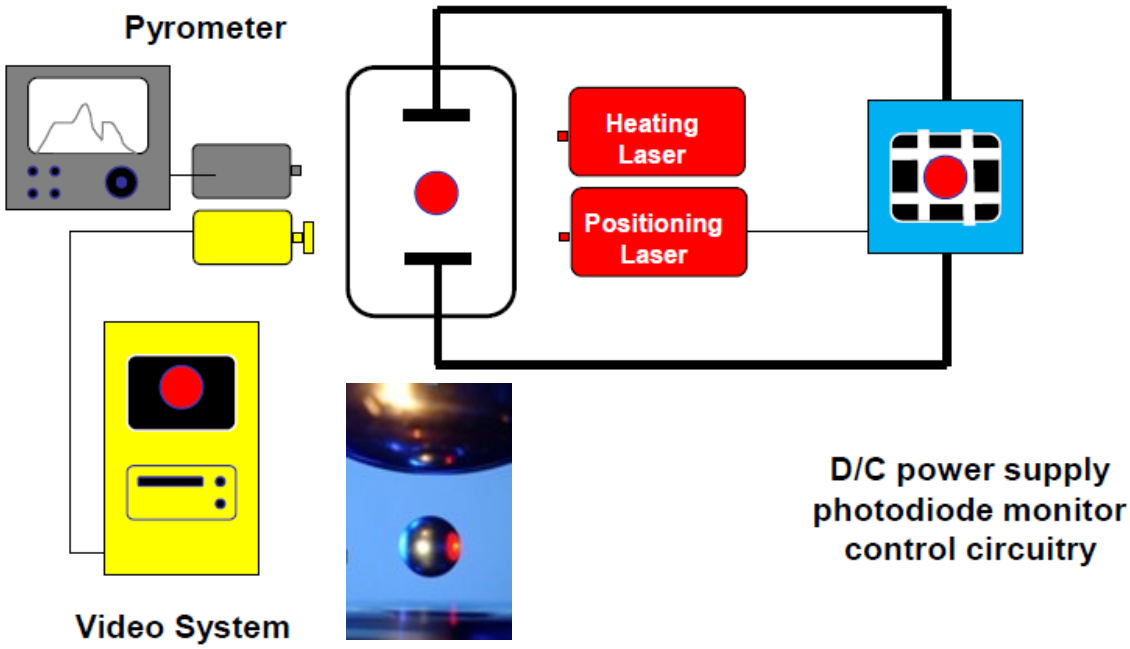

Figure 2: Electrostatic Levitation (ESL)

2.2 Effects of Internal Convection on Solidification

While the levitated molten ferritic alloys are solidifying, a two-steps double recalescence process could follow. First, the metastable ferrite phase (BCC, Body-Centered Cubic) forms from the undercooled liquid, and after a delay time, the alloys become to be the stable austenite phase (FCC, Face-Centered Cubic). Figure 3 shows the phase diagram of iron-cobalt, which is obtained from Thermo-Calc. The composition of cobalt continuously changed from 0% to 100%, the liquidus phase, FCC and BCC phase is marked in the plot, and the red curve is the projected from BCC phase as the metastable BCC. For molten $Fe_{50}Co_{50}$ liquid above the molten temperature,

it would deep undercools from the superheated status, and achieves the metastable BCC phase first, and after a delay time it achieves the stable FCC phase and solidifies.

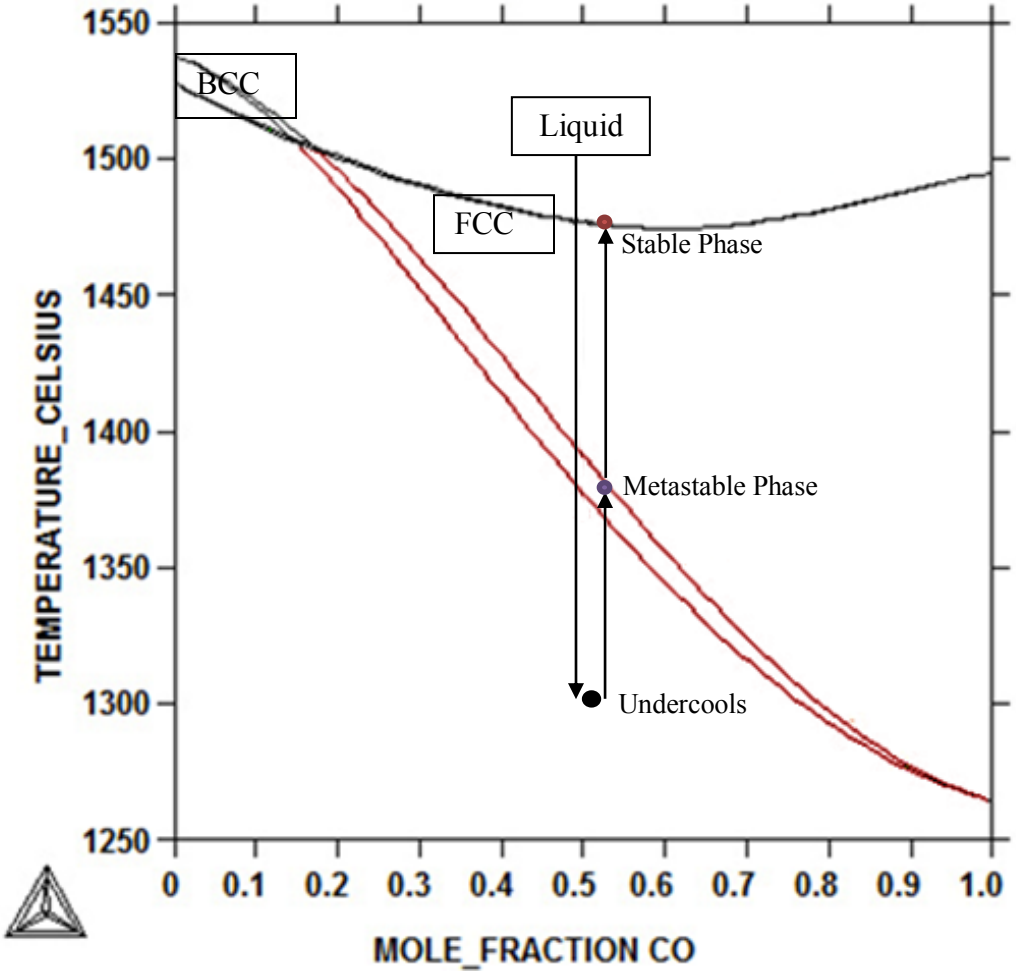

Figure 3: Fe-Co Metastable Phase diagram

Previous research showed that the internal convection flow has great effect on the lifetime of the metastable phase [1]. In electrostatic levitation (ESL) experiments, the internal convection is mainly driven by Marangoni flow induced by a non-uniform heating flux from the laser source, which is used to melt and heat the samples [3]. In electromagnetic levitation (EML) experiments, the electromagnetic force dominates the internal convection, which is induced by the alternating current through the coils that

are used to position and heat the samples. The delay time in ground ESL is much larger than ground EML, which means the magnetohydrodynamic flows in EML must strongly influence the lifetime of the metastable phase as it can be seen by Figure 4, which gives an example of $Fe_{60}Co_{40}$ [22].

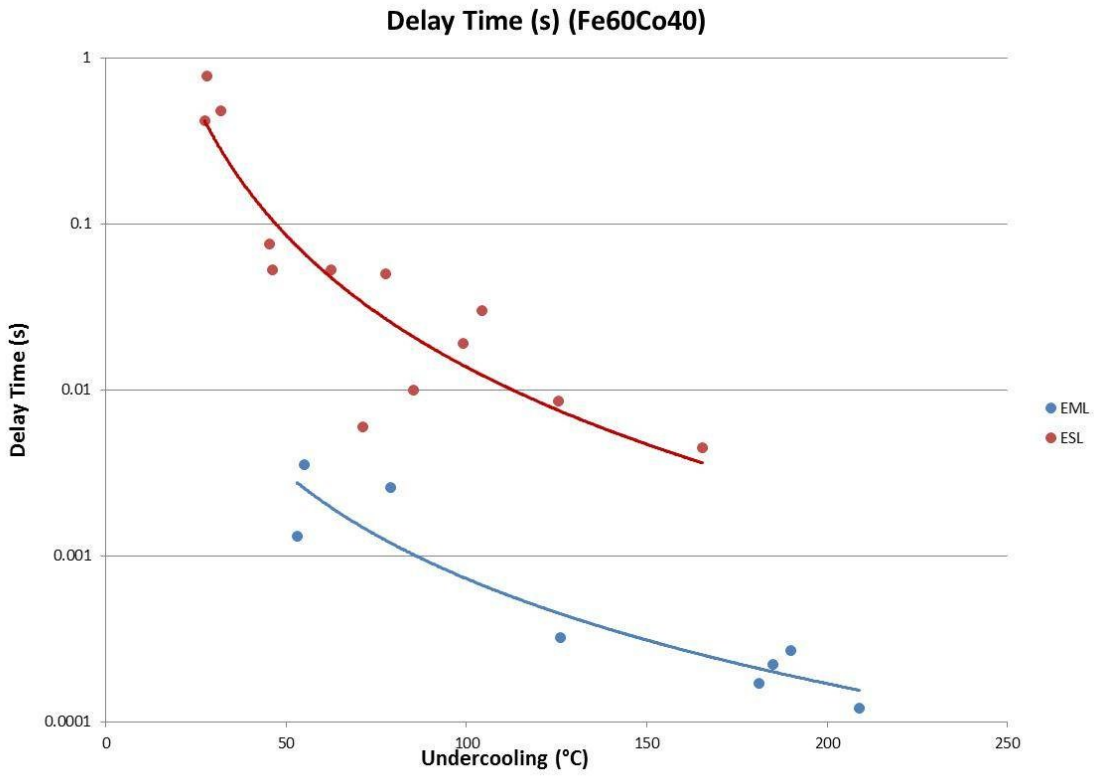

Figure 4: Delay Time of $Fe_{60}Co_{40}$ for ground-based ESL and EML testing

For the mechanism of how the convection flow influences the dendrites in the metastable phase, classical nucleation theory can be used to show that the nucleation of the stable phase would be triggered by collision of the dendrites [6], The free stream flow causes mechanical damage to the growing dendrites and leads to dendrite collision [2]. If the dendrites' primary arms are bent, the secondary arms of adjacent dendrites would collide with each other and form some narrow crevices. In these crevices, a

smaller volume is required to form a nucleus with critical radius and less energy is needed to nucleate the stable phase. If secondary nucleation happens early in the process, the lifetime of the metastable phase would be too short to be fully transformed, resulting in a mixed microstructure of dendrites. The primary metastable front may even be overwhelmed by the growth of the stable phase dendrites. Longer delay time could lead to finer microstructure [5].

Eutectic ternary steel alloys behave similarly to the peritectic FeCo binary in that the delay between primary and secondary phases is influenced by convection [4]. Microstructures are significantly influenced by the solidification path with very different structures evident where single and double recalescence occurs locally within the same sample. In Figure 5 [4], the microstructure of a $Fe_{72}Cr_{12}Ni_{16}$ sample is presented. Figure 5 (a) shows the grain refined region formed from primary ferrite solidification, and Figure 5 (b) shows dendritic structure formed from primary austenite solidification.

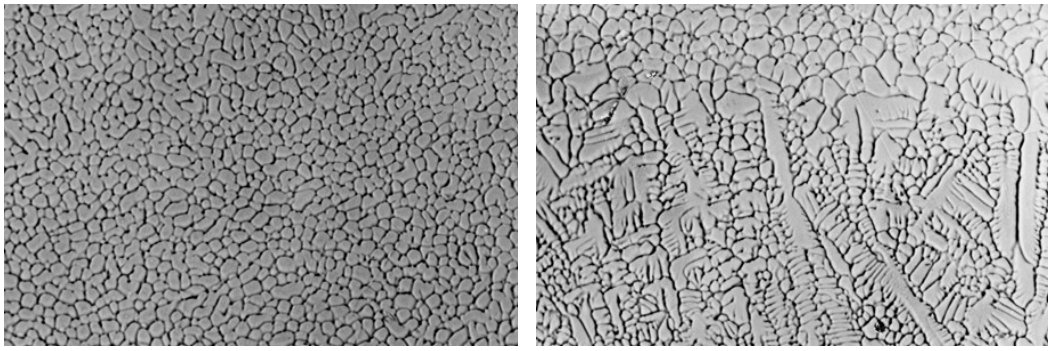

(a) Double Recalescence (b) Single Recalescence

Figure 5: Solidification Microstructures for $Fe_{72}Cr_{12}Ni_{16}$ (wt%) [4]

To characterize of the convection flow, the Reynolds number should be evaluated to determine if the status of the flow is laminar or turbulent. In fluid flow, the Reynolds number measures the ratio of inertial forces to viscous forces, which is defined as $\mathrm{Re} = \rho UD/\mu$, where ρ and μ is the density and viscosity of the fluid, U is the flow velocity, and D is the characteristic length, here it refers to the sample's diameter. While the flow has low Re, the viscous effect dominates and the flow is laminar; while the flow has high Re, the inertial effect dominates and the flow can turn out to be turbulent.

Figure 6 [4] shows the ranges of convection velocity and Reynolds number of steel, for electromagnetic levitation experiments in microgravity, flight mission MSL-1, electromagnetic levitation experiment on the ground (ground EML), and electrostatic levitation experiment on the ground (ground ESL). In ground ESL, the sample size is 2 mm diameter; in microgravity EML, the sample with 6 mm, 7 mm, and 8 mm diameter is investigated. The laminar-turbulent transition point is around 525.

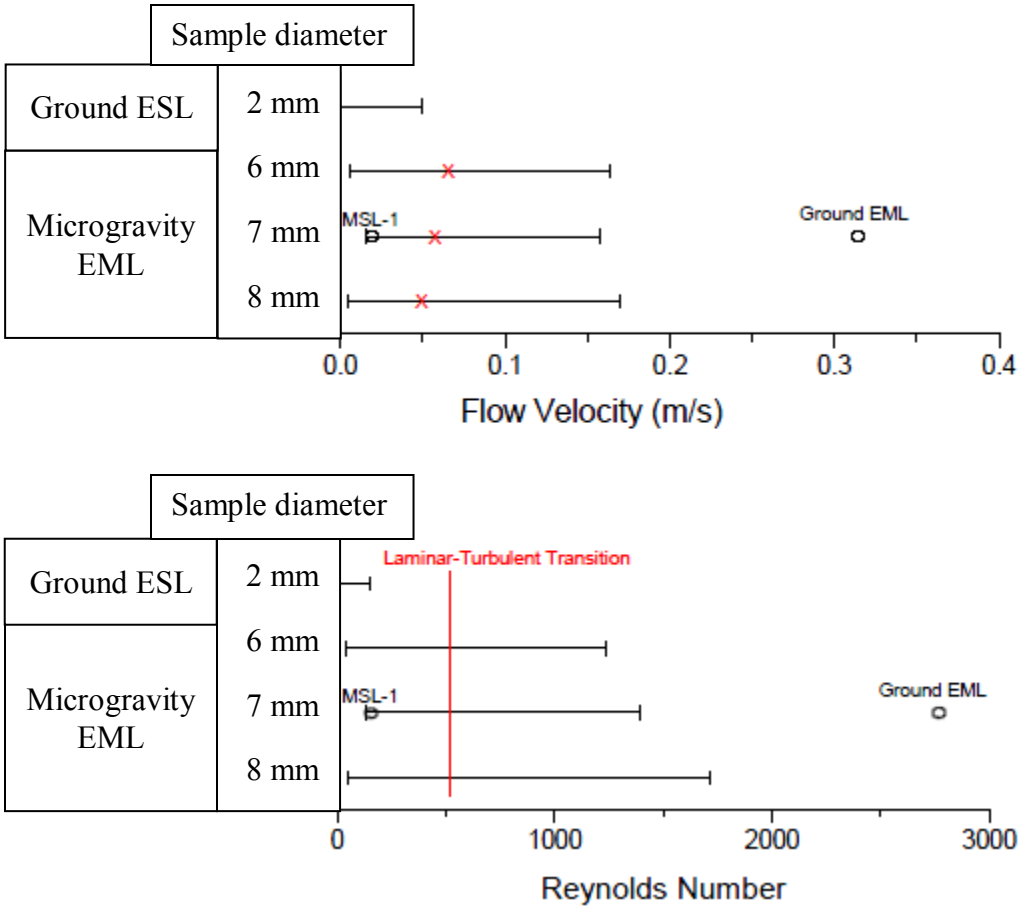

Figure 6: Ranges of Velocity and Reynolds Number of Steel for Microgravity EML, ground EML, and ground ESL [4]

In agreement with the behavior observed in Figure 4, the convection velocity in ground EML is around ten times larger than ground ESL within a narrow range, leading to completely laminar and turbulent flow separately, since it is basically Marangoni flow in ground ESL test that has much lower flow velocity, and in ground EML the internal driven forces of the fluid flow is very large due to the electromagnetic field that position the sample. For the molten samples in microgravity EML, only minimum positioning is required, and the electromagnetic driven forces inside the molten sample

can be controlled that the internal flow could achieve a wide range of velocities and Reynolds numbers.

2.3 Magnetohydrodynamics Model

Magnetohydrodynamics (MHD) descries the phenomenon that currents are induced to conductive fluid in an electromagnetic field, and electromagnetic body forces are introduced to the fluid correspondingly.

The magnetohydrodynamics of levitated droplets includes three interacting phenomena: the electromagnetic force field inside the drop, the free surface shape of the drop, and the fluid flow inside the drop [7].

A simplified form (magnetoquasistatic) of Maxwell's equations is employed to describe the electromagnetic field [8],

$$\begin{cases} \nabla \times \vec{H} = \vec{J} \\ \nabla \cdot \vec{B} = 0 \\ \nabla \cdot \vec{E} = -\dfrac{\partial \vec{B}}{\partial t} \end{cases} \tag{1}$$

where $\vec{J}$ is the induced current, $\vec{H}$ is the magnetic field, $\vec{B}$ is the magnetic flux density, and $\vec{E}$ is the electric field. The electromagnetic body force which is also known as Lorentz force is written as,

$$\vec{F} = \vec{J} \times \vec{B} \tag{2}$$

The calculation of the distribution of the electromagnetic body force used the method of mutual inductances, which is shown in [8]-[11] as cited in [7]. This method discretizes

the object into many elements and calculates the current in each element. A subroutine was developed by Hyers [7] to calculate electromagnetic force with inputs of current, frequency, coil geometry, sample size and electrical conductivity.

In [7] and [12], Hyers looked at flight and ground based fluid convection in electromagnetically levitated $Pd_{82}Si_{18}$ and $Fe_{72}Cr_{12}Ni_{16}$ droplets with TEMPUS Coil as shown in Figure 7.

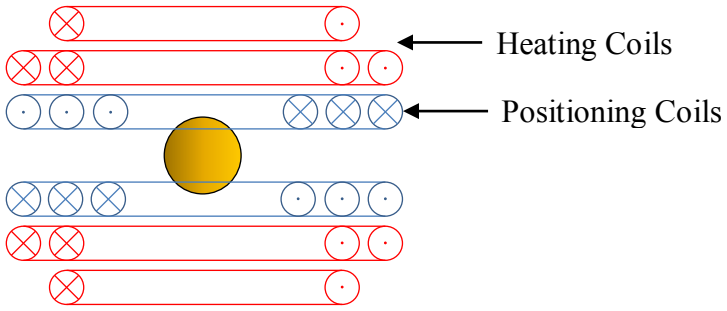

Figure 7: TEMPUS Coil Geometry [13]

The streamlines and velocity for both laminar and turbulent flow can be calculated with a CFD package, and the maximum convection velocity can be determined. The results are shown in Figure 8 [12]. Figure 8 (a) shows streamlines and velocity for laminar flow inside levitated $Pd_{82}Si_{18}$ droplet in microgravity EML with maximum velocity of 13 cm/s, Figure 8 (b) shows streamlines and velocity for turbulent flow inside levitated $Fe_{72}Cr_{12}Ni_{16}$ droplet in 1-g EML with maximum velocity of 32 cm/s.

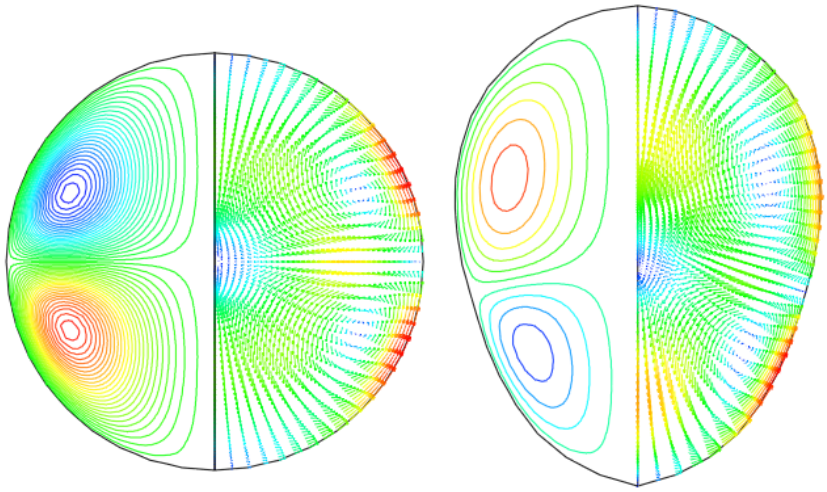

(a) $Pd_{82}Si_{18}$ droplet (b) $Fe_{72}Cr_{12}Ni_{16}$ droplet

Figure 8: Calculated streamlines and flow velocity [12]

3 Modeling

3.1 Problem Description

The fluid flow inside molten alloys droplet can be assumed to be steady-state and incompressible, which is governed by Navier-Stokes equations expressed in the following dimensionless form,

$$\begin{aligned} &\nabla^* \cdot \vec{u}^* = 0 \\ &\frac{\partial \vec{u}^*}{\partial t^*} + \vec{u}^* \cdot \nabla^* \vec{u}^* = -\nabla^* P^* + \frac{1}{Re} \nabla^{*2} \vec{u}^* + \vec{F}^* \end{aligned} \tag{3}$$

where $\vec{u}^*$ is the velocity vector, P^* is the pressure, and $\vec{F}^*$ is the source term which is known as electromagnetic body force defined in section 2.3. Reynolds number is defined to characterize the fluid flow, as follows,

$$Re = \frac{\rho U D}{\mu} \tag{4}$$

where ρ is the density, U is the flow velocity, D is the diameter of the droplet, and μ is the dynamic viscosity.

In the model, the flow is assumed to be steady state, i.e. time independent, hence $\frac{\partial}{\partial t} = 0$, and this assumption will be discussed in the following part. The flow is incompressible, the density ρ is a constant with the same temperature. Thus, in two-dimensional Cartesian coordinate, the Navier-Stokes equations are written as follows,

$$\begin{cases} \rho \left(u_x \dfrac{\partial u_x}{\partial x} + u_y \dfrac{\partial u_x}{\partial y} \right) = -\dfrac{\partial P}{\partial x} + \mu \left(\dfrac{\partial^2 u_x}{\partial x^2} + \dfrac{\partial^2 u_x}{\partial y^2} \right) + F_x \\ \rho \left(u_x \dfrac{\partial u_y}{\partial x} + u_y \dfrac{\partial u_y}{\partial y} \right) = -\dfrac{\partial P}{\partial y} + \mu \left(\dfrac{\partial^2 u_y}{\partial x^2} + \dfrac{\partial^2 u_y}{\partial y^2} \right) + F_y \end{cases} \tag{5}$$

With continuity conditions,

$$\frac{\partial u_x}{\partial x} + \frac{\partial u_y}{\partial y} = 0 \tag{6}$$

Where $u_x(x, y)$ is the velocity in x-direction, and $u_y(x, y)$ is the velocity in y-direction. In x and y direction respectively, the term $\left(u_x \frac{\partial u_x}{\partial x} + u_y \frac{\partial u_x}{\partial y}\right)$ and $\left(u_x \frac{\partial u_y}{\partial x} + u_y \frac{\partial u_y}{\partial y}\right)$ in the equations describes the acceleration of flow convection, $\mu\left(\frac{\partial^2 u_x}{\partial x^2} + \frac{\partial^2 u_x}{\partial y^2}\right)$ and $\mu\left(\frac{\partial^2 u_y}{\partial x^2} + \frac{\partial^2 u_y}{\partial y^2}\right)$ introduced the viscous effects into the flow, $\frac{\partial P}{\partial x}$ and $\frac{\partial P}{\partial y}$ is the pressure gradient since the pressure $P(x, y)$ changes with different flow field. For the MHD model, source term F_x is the electromagnetic body forces in x-direction, and F_y is the electromagnetic body forces in y-direction, which are calculated separately.

For boundary conditions, the droplet is assumed to be undeformed with fixed free surface, i.e. a sphere shape, and there is flow crosses the wall.

$$u_r^*|_{r^*=1} = 0 \tag{7}$$

Where u_r^* is the non-dimensionless radial velocity, r^* is the non-dimensionless radial coordinate. At the boundary, the flow velocity is zero as the velocity vector is normal to the boundary of the sphere.

Slip wall boundary conditions is applied, i.e. shear stress on the wall equals zero,

$$\tau^* \cdot \vec{\imath}_t|_{r^*=1} = 0 \tag{8}$$

Where τ^* is the non-dimensionless shear stress, and $\vec{\imath}_t$ is the tangent unit vector.

The transient of the time scale should be evaluated to verify the steady-state assumption in the model, by comparing the time to achieve internal and external equilibrium. For the internal thermal equilibrium, Fourier number is defined by,

$$F_0 = \frac{\propto t_1}{L^2} \tag{9}$$

Where t_1 is the characteristic time to achieve internal thermal equilibrium, L is the characteristic length that the heat conduction from the boundary to the inner center, here it corresponds to the sample's radius which is 3.25 mm, and $\propto = \frac{k}{\rho C_p}$ is the thermal diffusivity. At Tm+70, the density ρ is 7435 kg/m^3 for molten $Fe_{50}Co_{50}$ according to Table 1 in section 3.3, the thermal conductivity k is 33.3 W/(m·K) for molten Fe, and 31.9 W/(m·K) for molten Co [24], the heat capacity C_p is 748.5 J/(kg·K) for molten Fe, and 685.2 J/(kg·K) for molten Co [25]. Thus, the thermal diffusivity $\propto$ of molten $Fe_{50}Co_{50}$ is within a range from $5.7 \cdot 10^{-6}$ m^2/s to $6.5 \cdot 10^{-6}$ m^2/s. While $F_0 = 1$, the time t_1 is written as,

$$t_1 = \frac{L^2}{\propto} \tag{10}$$

Thus, t_1 is around 1.62 s to 1.84 s allowing the heat conduction to occur.

Refer to the sample's temperature-time profile in the EML experiment, which will be discussed in details in section 5.2, during the process that the sample is melted and superheated to the highest point T_1, and cooled down to an equilibrium temperature or achieve the recalescence plateau T_2, the relaxation time to achieve external thermal equilibrium is defined as t_2, which describes the time needed from T_1 to T_2', where T_2' is a value between T_1 and T_2.

$$T_2' - T_2 = (T_1 - T_2)e^{-\frac{t}{t_2}} \tag{11}$$

While it is at the relaxation time $t = t_2$, $\frac{T_2' - T_2}{T_1 - T_2} = \frac{1}{e} \cong 0.37$. Thus, the t_2 can be defined as the period that the sample's temperature drops down from the highest point to 37% of it. Depends on the different cooling rate with different power settings of the heater, t_2 is around 8 s to 15 s.

The ratio between t_1 and t_2 is used to evaluate the effect of internal relaxation time and external relaxation time to achieve an equilibrium. Based on the above estimated result, t_1 / t_2 is expected to be around 0.1 to 0.2, which means the time to achieve internal equilibrium is much smaller than external equilibrium; hence the influence of internal relaxation time could be neglected in the model. The model can be assumed to be steady state.

3.2 Levitation Coil Geometry

Current work will concentrate on simulation of convection flow inside levitated $Fe_{50}Co_{50}$ alloy in microgravity EML with the new coil geometry SUPOS as shown in Figure 9, and define the accessible range of the convection velocity during actual EML experiments.

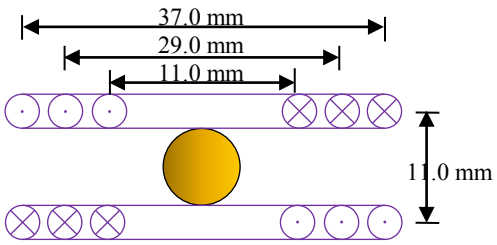

Figure 9: SUPOS Coil Geometry [13]

Compared to the previous TEMPUS coil, SUPOS has only one set of coils instead of two separated ones, and it is more efficient in heating the sample since the coils are closer to the sample. SUPOS coil was designed to position and heat simultaneously by setting the currents at different frequencies for positioning and heating.

In SUPOS, the diameter of the inner, intermediate, and outer coils is 11.0 mm, 29.0 mm, and 37.0 mm respectively. The height between upper and lower coils is 11.0 mm. More details about SUPOS coil can be found in [14].

3.3 Material Properties

The thermophysical properties are critical in simulation. The molten alloy's density and viscosity varies as function of temperature that lead to different results under different power settings. The electrical conductivity of $Fe_{50}Co_{50}$ is assumed to be constant, which is presented in [15]. The density and viscosity value of molten $Fe_{50}Co_{50}$ at its melting point 1750 K is from [16] and [17] respectively, as well as their fitted functions varying with temperature, which are shown in table 1 and Figure 10.

$Fe_{50}Co_{50}$ Properties	**Values at Tm (1750K)**	**Value varies with Temperature (K)**
Density (kg/m^3)	7515	$\rho = 9510 - 1.14 \cdot T$
Viscosity (Pa·s)	5.94×10^{-3}	$\mu = 10^{-3.6615+2512/T}$
Electrical Conductivity (1/Ω·m)	7.50×10^{5}	

Table 1: Material Properties of $Fe_{50}Co_{50}$

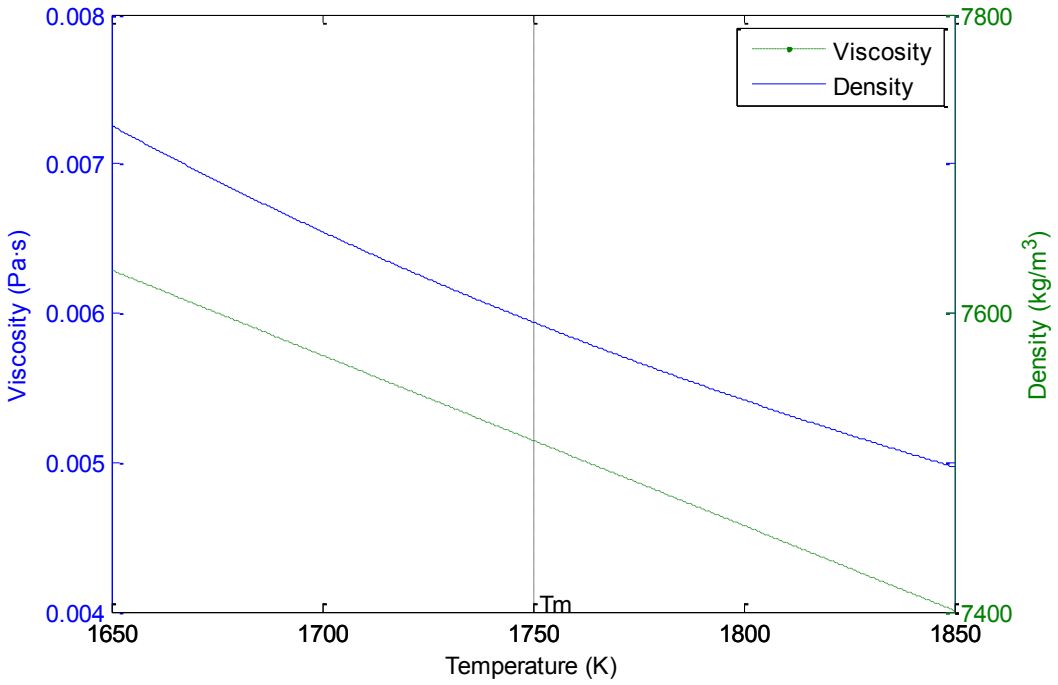

Figure 10: $Fe_{50}Co_{50}$ Thermophysical Properties

Compared to the density showed in Brillo's [23], $Fe_{50}Co_{50}$ has density of 7430 kg/m^3 at Tm, with density slope of 0.748 kg/(m^3·K), there is around 1.1% difference from Watanabe's [16]. At Tm-200 and Tm+200, there is around 3.8% and 4.0% difference respectively between Brillo's and Watanabe's density data, and the density changes around 6.0% within this range. Thus, the error in density does not significantly influence the simulation, neither the effect of thermal expansion.

3.4 Simulation with ANSYS-Fluent®

3.4.1 Meshing

In a microgravity environment, surface tension keeps the droplet free surface in a nearly spherical shape, and the magnetohydrodynamics simulation shape can be

assumed to be a sphere. For convenience without loss of accuracy, a two-dimensional axisymmetric model in semi-spherical shape is applied. The droplet model is a semi-sphere with 6.5 mm diameter, and meshed with 550 cells and 591 nodes as shown in figure 11.

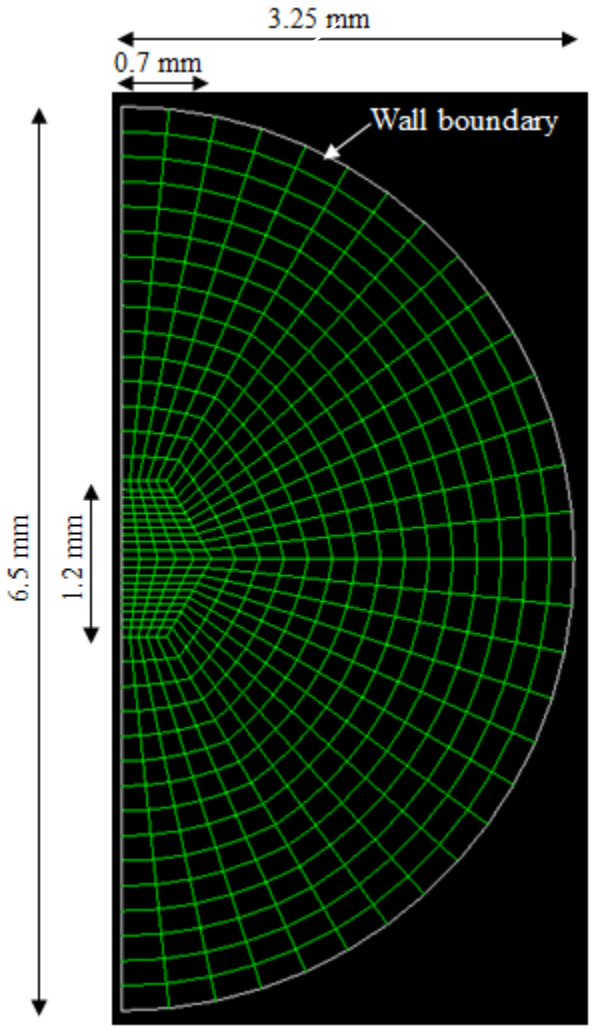

Figure 11: 2D Axisymmetric Model for $Fe_{50}Co_{50}$ Droplet

Considering the skin effect, there is tendency that the alternating current is distributed near the surface of a conductor, and the electromagnetic forces will dominate the affected area. The skin depth is used to characterize the skin effect, which is the depth blow the conductor's surface defined as follows,

$$\delta = \sqrt{\frac{2}{\omega\sigma\mu}} \tag{12}$$

where ω is the angular frequency of the current, σ is the electrical conductivity, μ is the permeability. The skin depth of current model is around 2.5 mm when the frequency of current is 350 kHz, and the fraction of the skin depth to radius is 76.9%. Since the electromagnetic forces will occupy most of the sample body, the mesh pattern fits the electromagnetic forces distributed in this regime, and uniform grid is appropriate.

To verify the accuracy of the results with current mesh size, simulation is performed with increased number of cells in the mesh- 88, 198, 352, 550, and 792 cells, as shown in Figure 12 (a)-(e). Figure 13 (a) shows the simulation result with laminar model at molten temperature and 20 A heating current; Figure 13 (b) shows the simulation result with turbulent model at molten temperature and 50 A heating current. The results show that the value of max flow velocity becomes stable when the mesh includes more than 352 cells, while the number of iterations during computation increases significantly with the mesh size. Thus, it is appropriate to utilize the mesh with 550 cells to ensure the accuracy of the computation without loss of computational efficiency.

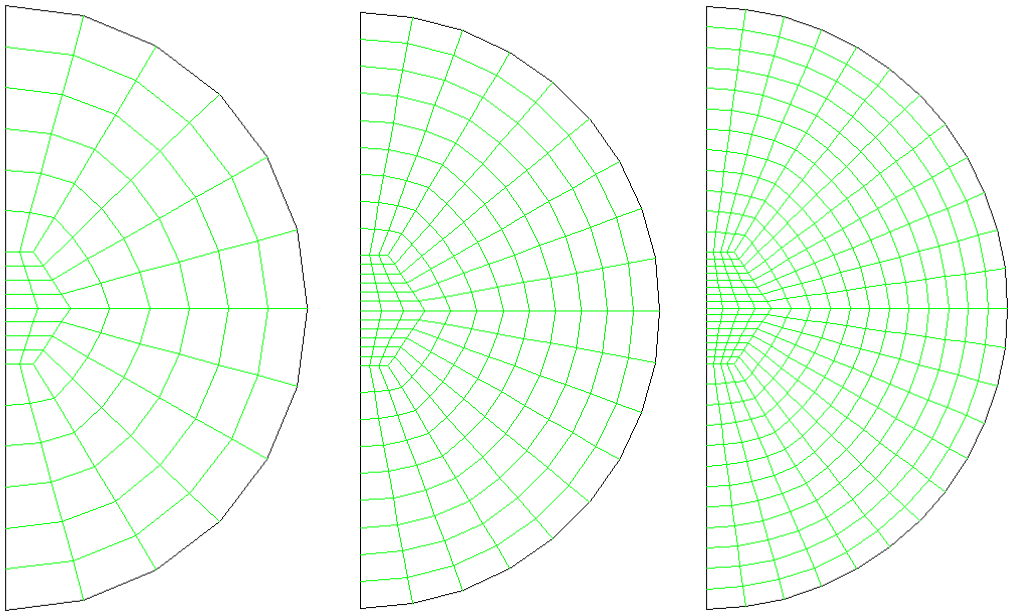

(a) 88 cells (b) 198 cells (c) 352 cells

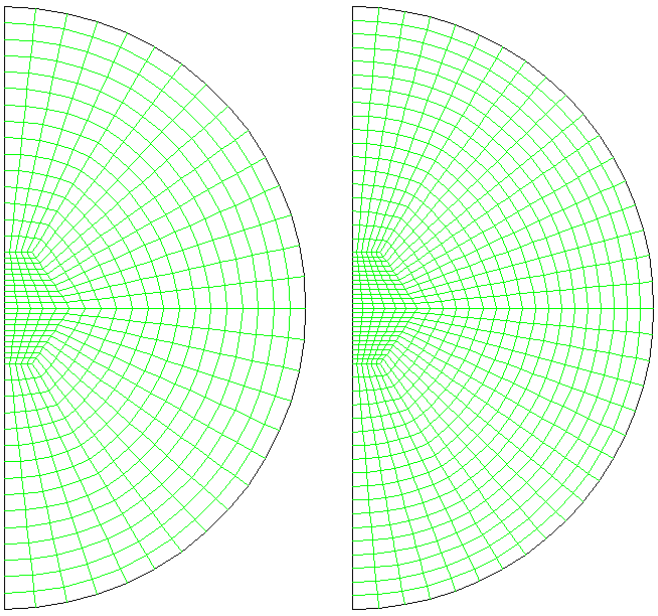

(d) 550 cells (e) 792 cells

Figure 12: Mesh with increased number of cells

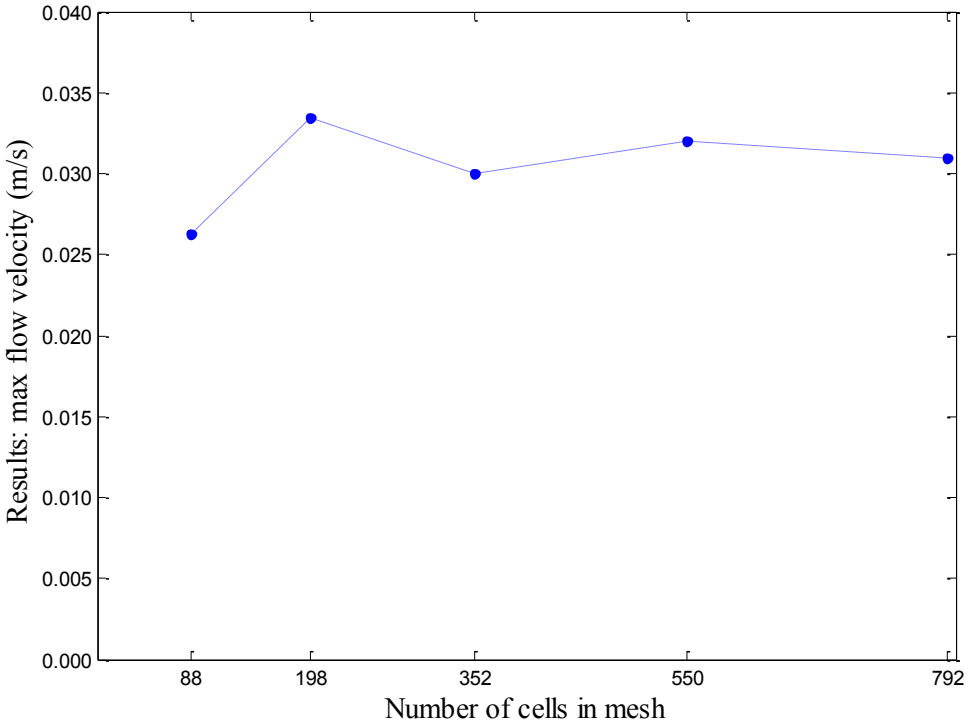

(a) Laminar model

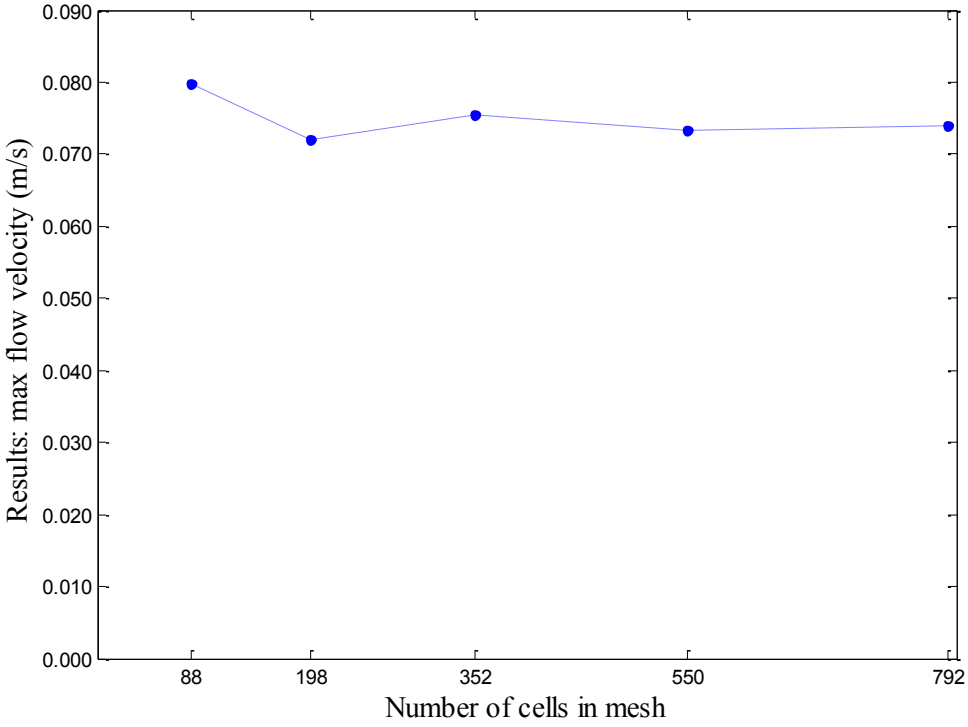

(b) Turbulent model

Figure 13: Simulation Results vs. Mesh size

3.4.2 Source Term

Electromagnetic body force is calculated with given positioning/heating current, coil geometry, sample size, and electrical conductivity of the material by the subroutine which was developed in previous research [8]. With the method of mutual inductance, 400 elements are generated in a semi-sphere with a ring-shaped distribution, and the electromagnetic body force is calculated in each element.

The current mesh contains 550 cells, and the value of source term, i.e. the electromagnetic body force should be evaluated in each cell. Bilinear interpolation is applied to calculate the electromagnetic body force in the current mesh based on the results from the subroutine Mags (Hyers [8]). A program in C is developed to realize this function, and interpreted by ANSYS-Fluent as user-defined function (UDF).

Figure 14 (a) shows the distribution of electromagnetic body forces calculated in the subroutine program Mags for 6.5 mm diameter $Fe_{50}Co_{50}$ using SUPOS coil that the positioning/heating current is 145 A/0 A. Figure 14 (b) shows the interpolated electromagnetic body forces using the current mesh, there is a source term in each cell of the mesh.

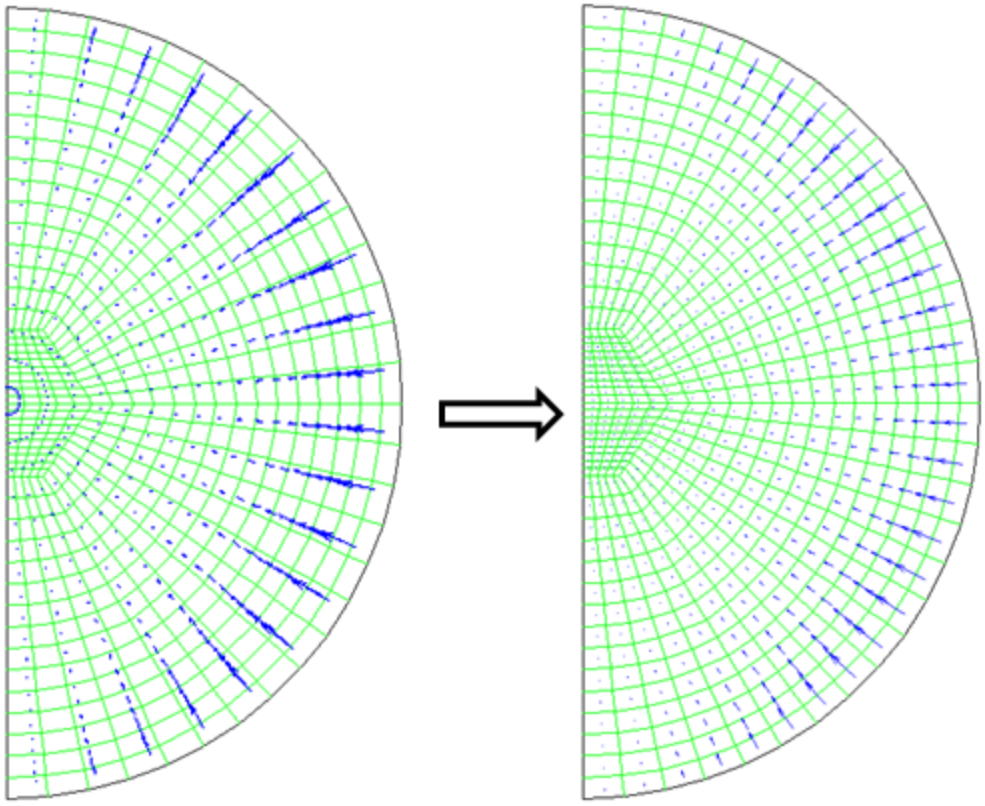

(a) Calculated forces in subroutine Mags (b) Interpolated forces in UDF

Figure 14: Electromagnetic Body Force as Source Term

Figure 15 shows the schematic of interpolation process. The vector of electromagnetic body forces are calculated from subroutine Mags, the values, directions and positions of the forces are known.

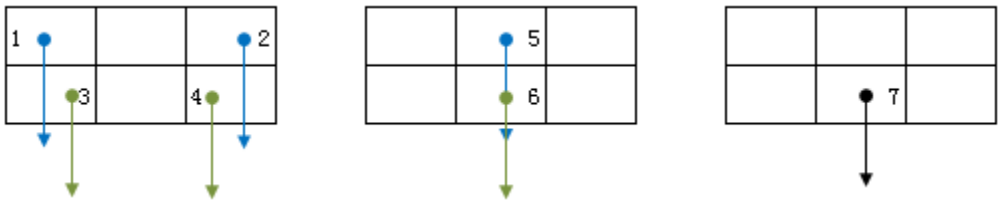

(a) Forces need to be interpolated (b) First interpolation (c) Second interpolation

Figure 15: Schematic of interpolation process

Based on the calculated forces from Mags, we interpolate the forces that position in the center of each cell in current mesh. Figure 15 (a) schematically shows the calculated forces 1 to 4, the force in lower center cell needs to be interpolated. In Figure 15 (b), force 5 is linearly interpolated between force 1 and force 2; force 6 is linearly interpolated between force 3 and force 4. In Figure 15 (c), the force 7 is positioned in the center of the cell, which is linearly interpolated between force 5 and force 6.

3.4.3 Solution Methods

The simulation runs were evaluated both with both a laminar model and a turbulence model. The solver is set to be pressure-based and steady state with 2D axisymmetric space. The solution methods in ANSYS-Fluent are presented in Table 2. With steady state assumption, the flow is fully-developed and time-independent. The flow is also assumed to be incompressible, thus the pressure-based solver is appropriate while the density-based solver is basically used to solve compressible problem.

Solver Setting		**Method/ Scheme**
Turbulence Model		RNG k-epsilon
Pressure-Velocity Coupling Scheme		SIMPLEC
Interpolation Scheme	Gradient	Green-Gauss Node Based
	Pressure	Body Force Weighted
	Momentum	Second Order Upwind
	Turbulent Kinetic Energy	Second Order Upwind
	Turbulent Dissipation Rate	Second Order Upwind

Table 2: Solution Methods in ANSYS-Fluent

For the solver [26], pressure-velocity coupling refers to the numerical algorithm which uses a combination of continuity and momentum equations to derive an equation for pressure, and SIMPLEC is based on the semi-implicit method for pressure-linked

equations which provides faster convergence. Different schemes are applied to interpolate the values of different terms to each cell or node. For the pressure, the body force weighted scheme is applied, which is effective with large body forces and highly swirling flows. The gradients of solution variables, such as the velocity derivatives at the cell center, can be determined by interpolation approaches. Here the Green-Gauss node based scheme is applied which provides accurate and computationally intensive. For momentum, turbulent kinetic energy, and turbulent dissipation rate approximation, we apply the upwind scheme to interpolate their values on the cell faces. Based on these physical values in the center of the cells, the values on the faces of the cells can be derived through a Taylor series expansion. In first order upwind, the value on a certain cell face can be computed as the sum of the cell-centered value in its upstream cell and the gradient times displacement from the center of upstream cell to the face of current cell. Compared to first order upwind, the second order upwind uses the values in another two upstream cells to calculate the values on faces of the current cell, and provides second order accuracy. Additionally, the second order upwind is stable and will not induce oscillations of the solutions.

For turbulence model, [18] discussed several methods and showed that RNG variation of k-epsilon is the most effective one for simulation of the flow inside levitated molten alloy droplets and that is what was used in this research. Modeling turbulence is one of the most difficult problems in fluid dynamics, and solution of the Navier-Stokes equation usually requires numerically difficult approaches involving a set of simplification assumptions. The Reynolds averaged Navier-Stokes equations uses a

time-averaging method to define the fluid flow. The time-averaged velocity can be defined as,

$$\bar{u} = \lim_{T\to\infty} \frac{1}{T}\int_0^T u\, dt \tag{13}$$

The main idea of the Reynolds averaged Navier-Stokes equations is that the instantaneous velocity u can be decomposed to an averaged component $\bar{u}$ and the fluctuating component u'. The average of the fluctuating component is symbolized as $\overline{u'}$. Applying the time-averaging technique to the Navier-Stokes equations, the Reynolds averaged Navier-Stokes equations can be derived. In the derivation process, the convective term is decomposed into two parts $\rho\bar{u}_j \frac{\partial \bar{u}_i}{\partial x_j}$ and $\frac{\partial}{\partial x_i}(\rho\overline{u_i' u_j'})$ (indicial notation in multi-dimensions). Thus, the time-averaged Navier-Stokes equations, contains averaged viscous terms, and a Reynolds stress terms $\rho\overline{u_i' u_j'}$, which describes the additional stresses generated due to turbulent fluctuations. The k-epsilon turbulent model is a two-equation model based on the Reynolds averaged Navier-Stokes equations; it includes both a scalar turbulent kinetic energy k- equation and a scalar epsilon-equation representing the dissipation rate of turbulent kinetic energy. The turbulent kinetic energy is defined as $k = \frac{1}{2}\overline{u_\iota' u_\iota'}$, and dissipation rate is defined as $\varepsilon = \nu \frac{\partial \overline{u_\iota'}}{\partial x_j}\frac{\partial \overline{u_\iota'}}{\partial x_j}$ where ν is the kinematic viscosity. Generally, k and ε can be substituted into the Reynolds averaged Navier-Stokes equations, and we will obtain the k and epsilon equation after derivations. Specifically, the k-equation contains convective terms of k and $\bar{u}_j$, a turbulent transport term that is related to the viscosity and derivatives of $\overline{u_\iota'}$and k in a form of viscous stresses, a production term $\rho\overline{u_\iota' u_j'}\frac{\partial \bar{u}_\iota}{\partial x_j}$ that

corresponds to the Reynolds stress derived in Reynolds averaged Navier-Stokes equations, and dissipation term $\rho\varepsilon$. Similarly, the epsilon-equation contains the turbulent transport, production, and dissipation term. All these terms are functions involving the average of the fluctuating component of convection and are used to estimate the effect of turbulence. By numerically solving the k-epsilon equations, the time-averaged flow behavior can be evaluated, as well as the magnitude of turbulent fluctuations. The k-epsilon models are widely used to solve turbulent problems, and there are many different forms such as standard k-epsilon and RNG k-epsilon. Compared to the standard k-epsilon model, the RNG k-epsilon model uses renormalization group methods to renormalize the Navier-Stokes equations and modify the epsilon equation, and it can deal with wider ranges of turbulence length scale, with better performs regarding swirling flow, and transitional flow, thus allowing appropriate simulation of the convection flow and recirculations inside the levitated droplet.

4 Simulation Results

4.1 Convection Velocity vs. Current

Binder [19] measured the flow velocity near the surface of a $Co_{16}Cu_{84}$ droplet surface in ground-based EML experiment, and J. Lee, et al. [20] developed a MHD model, and compared the predicted and measured results. The model is validated by copper-cobalt and can be extended to iron-cobalt system.

In the simulation of a levitated $Fe_{50}Co_{50}$ droplet of 6.5 mm diameter, the maximum convection velocity inside the convection flow is studied with varying coil current and test temperature. The positioning current is fixed at 145 A, and the heating current is increased from 0 A to 150 A. The range of testing temperature is from 1400 K (undercooling 350 K) to 1950 K (superheating 200 K), while the $Fe_{50}Co_{50}$ liquidus temperature, Tm, is 1750 K.

The results are plotted in Figure 16 and Figure 17, where the convection velocity inside $Fe_{50}Co_{50}$ droplet is a function of current and temperature. Both laminar and turbulence models are utilized. The laminar model is used for heating current from 0 A to 30 A, and the turbulence model is used for heating current from 30 A to 150 A. The results show that how much coil current is needed for the molten droplet to achieve certain internal convection velocity under different temperature, and at what coil current the convection flow will be laminar or turbulent. These predictions can provide support for the experiments in future.

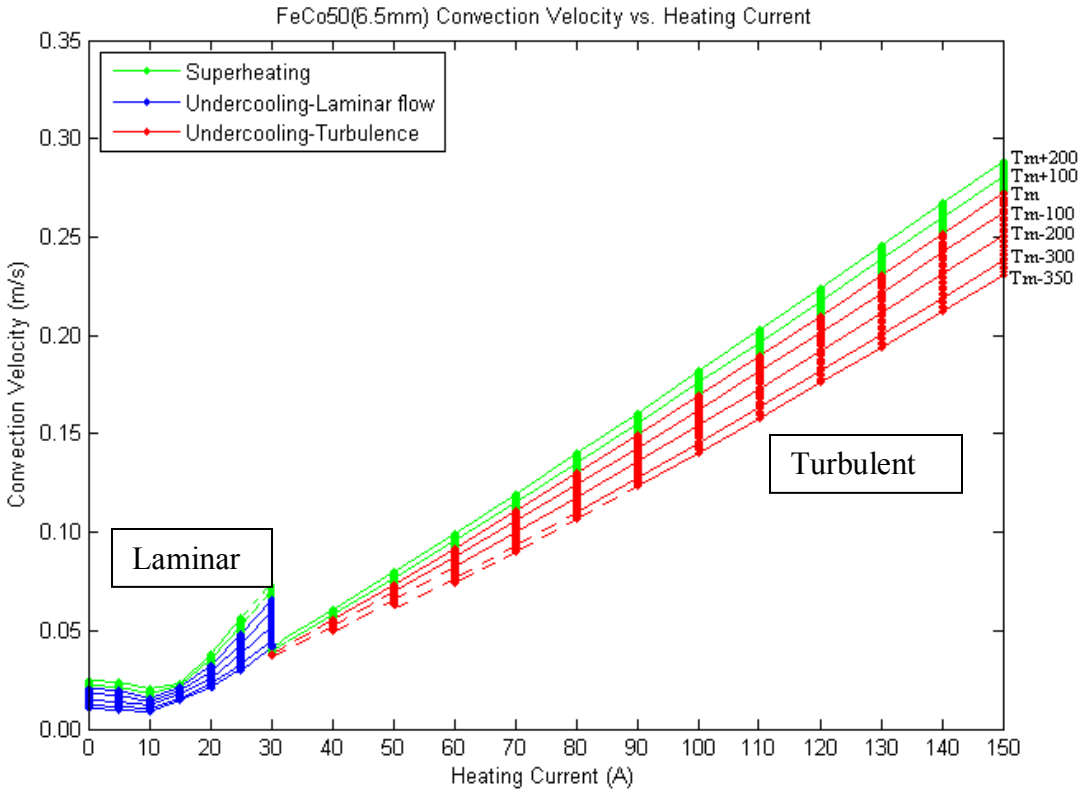

Figure 16: $Fe_{50}Co_{50}$ Droplet Convection Velocity vs. Heating Current

As shown in Figure 16, with a fixed current setting, the convection velocity is decreasing as the testing temperature goes down, since the density and viscosity of molten alloy is negatively correlated to temperature leading to higher density and viscosity at lower temperature and to slower convection velocity. The laminar-turbulent transition is in a range around Reynolds number of 525. We will refer to the Reynolds number which characterizes the flow in the following paragraph. In the turbulent case, the solid isothermal lines in Figure 16 show the convection velocity with a corresponding Reynolds number larger than 525, and the flow is expected to be turbulent; for the dash lines, the corresponding Reynolds number is within 300 to 525, the flow is not turbulent, but the turbulence is in the transition process between laminar and turbulent flow.

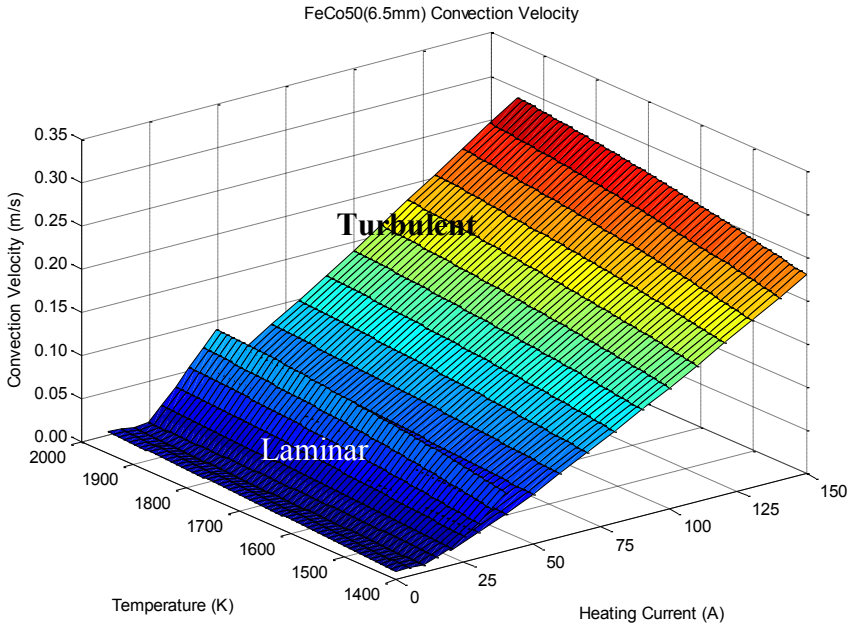

Figure 17: $Fe_{50}Co_{50}$ Droplet Convection Velocity (3D)

The Reynolds number is evaluated to characterize the convection flow. Figure 18 shows the Reynolds number characterizing the convection flow inside a levitated $Fe_{50}Co_{50}$ droplet. The estimated laminar-turbulence transition Reynolds number is around 525 [4]. In actual experiment, the internal convection velocity of the molten droplet is unknown, neither the Reynolds number. The achievable testing temperature normally ranges from Tm+150 to Tm-200; we computed more cases with wider temperature ranges to see the trend that convection velocity changes with the temperature. There is an overlap area between the laminar and turbulent model since the laminar-turbulent transition occurs in a regime of Reynolds number around 300 to 700, centered at 525, and the exact transition point is unknown in experiment. The dash lines in Figure 18 show the extended computation results of the laminar and turbulent

model, and these results provide an overall prediction of the laminar-turbulent transition behavior.

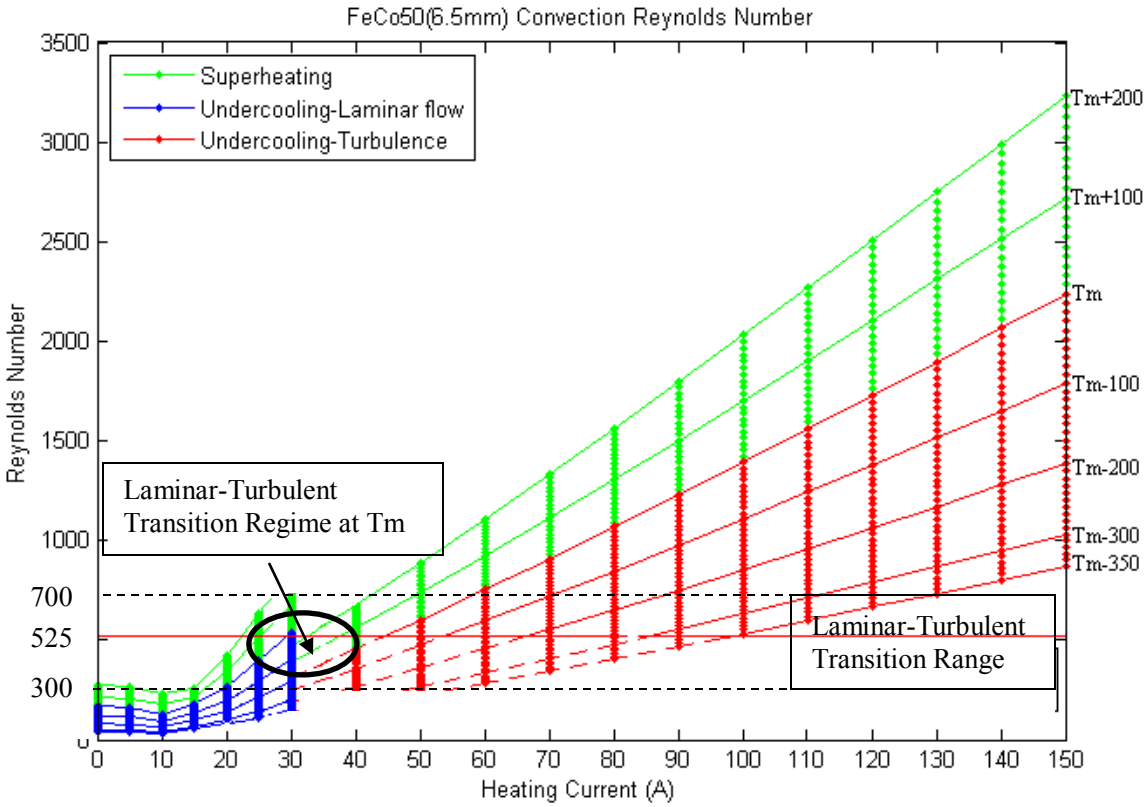

Figure 18: $Fe_{50}Co_{50}$ Droplet Reynolds Number vs. Heating Current

As shown in Figure 18, at the molten temperature of $Fe_{50}Co_{50}$ (Tm=1750 K), the convection flow stays laminar with heating current from 0 A to 25 A, and starts to show some turbulence at 30 A, afterwards it becomes completely turbulent from around 45 A. In general, the laminar-turbulence transition happens at the heating current around 25 A to 60 A depending on the testing temperature, normally from Tm+150 to Tm-200..

In the laminar regime, the convection velocity slightly decreases as the heating current increases from 0 A to 10 A, and shows a tendency of convergence at 15 A. With

heating current from 0 A to 15 A, the internal driven force and convection flow is positioner dominated. As the heating current increases, the effect of positioner is gradually cancelled out by the heater, and the internal driven force and convection flow becomes to be heater dominated since the heating current larger than 20 A. With heating current from 15 A to 30 A, the convection velocity steadily increases. In the turbulent regime, the convection velocity increases with the heating current, and they almost become proportional with heating current larger than 50 A.

4.2 Convection Flow Patterns

The internal convection of levitated $Fe_{50}Co_{50}$ droplet shows various flow velocity and flow patterns due to different current settings that lead to different patterns of electromagnetic body forces driving the flow. Figure 19 (a)-(l) shows the evolution of the flow patterns inside $Fe_{50}Co_{50}$ droplet of 6.5 mm diameter with corresponding distribution of electromagnetic body forces at molten temperature 1750 K, while the positioning current is fixed at 145 A and the heating current ($I_0{}^H$) increases from 0 A to 100 A, u_{max} stands for maximum convection velocity.

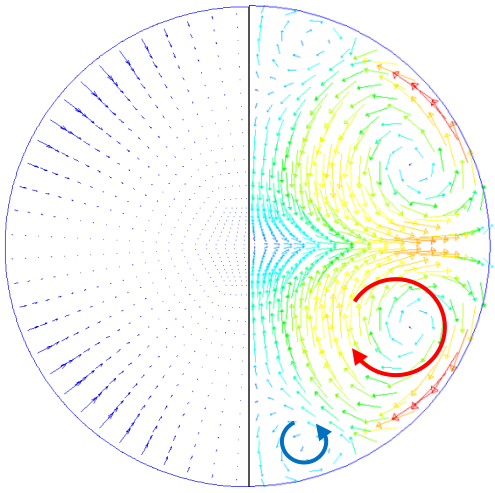

(a) $I_0{}^H$ =0 A, u_{max}=2.03 cm/s

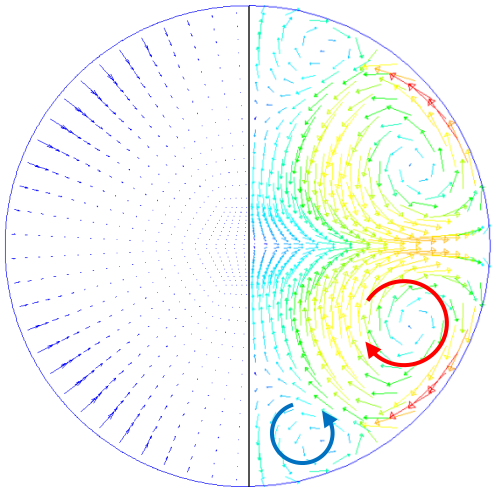

(b) $I_0{}^H$ =5 A, u_{max}=1.93 cm/s

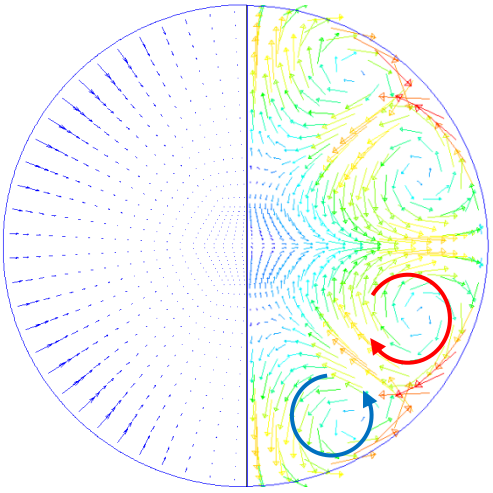

(c) I_0^H =10 A, u_{max}=1.58 cm/s

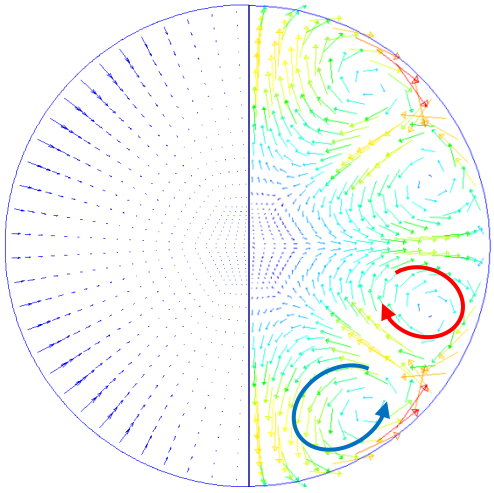

(d) I_0^H =11 A, u_{max}=1.69 cm/s

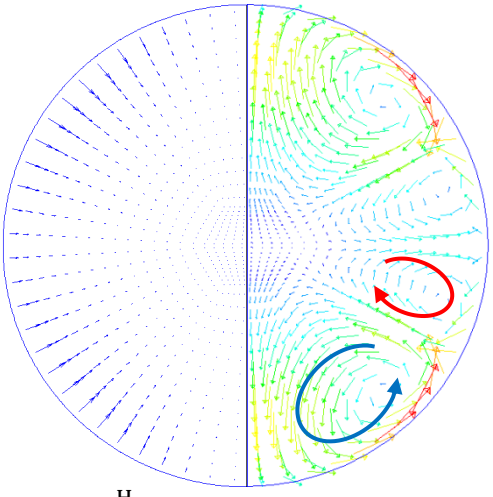

(e) I_0^H =12 A, u_{max}=1.81 cm/s

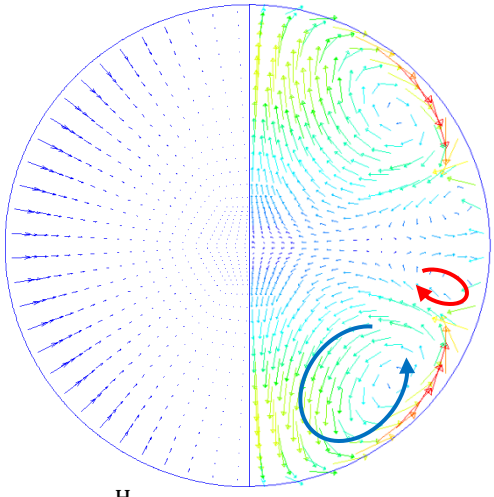

(f) I_0^H =13 A, u_{max}=1.92 cm/s

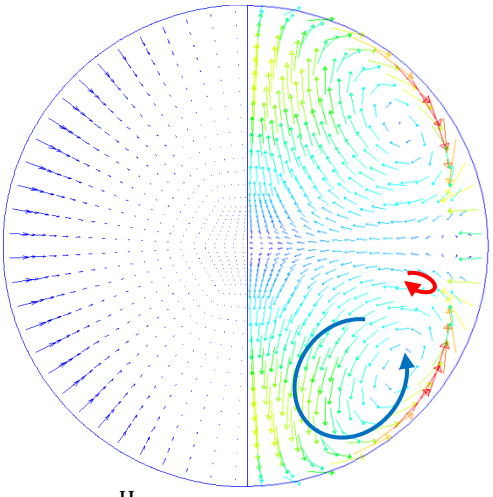

(g) I_0^H =14 A, u_{max}=2.03 cm/s

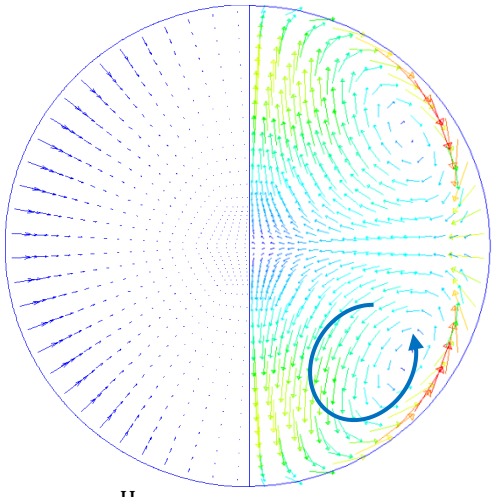

(h) I_0^H =15 A, u_{max}=2.14 cm/s

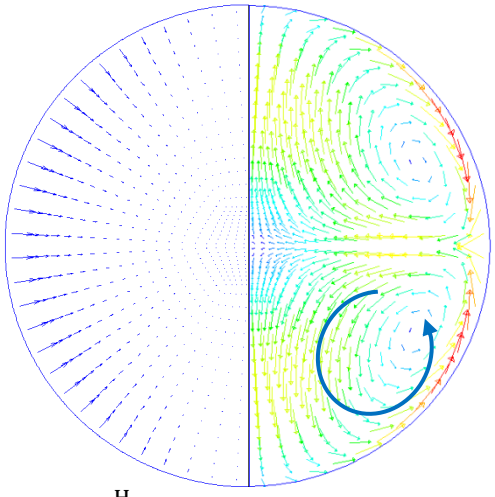

(i) I_0^H =20 A, u_{max}=3.24 cm/s

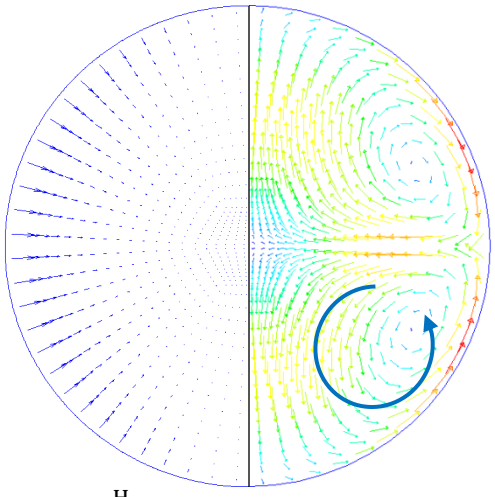

(j) I_0^H =30 A, u_{max}=3.82 cm/s

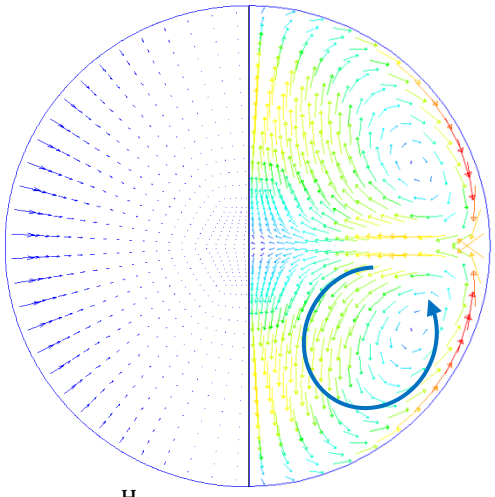

(k) I_0^H =50 A, u_{max}=7.33 cm/s

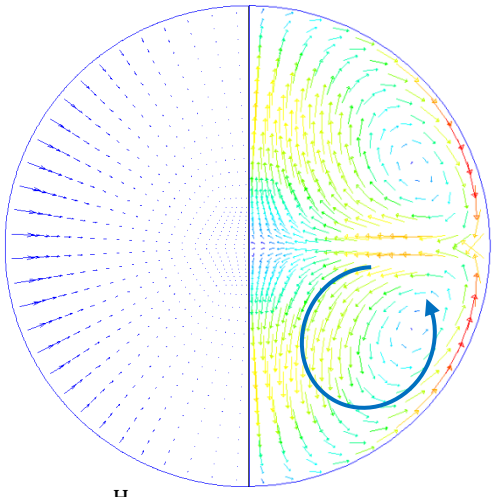

(l) I_0^H =100 A, u_{max}=16.95 cm/s

Figure 19: $Fe_{50}Co_{50}$ Droplet Flow Patterns

In Figure 19 (a), the heating current is 0 A, and the positioning current of 145 A is the primary source inducing the electromagnetic forces and driving the flow. The electromagnetic forces are largest at around ±45 degrees latitude in a quadruple field, and there is one large recirculation loop and another small recirculation loop in both of the upper and lower hemispheres. In Figure 19 (b)-(c), the heating current is increased to 10 A, and the electromagnetic forces induced from positioning current is superimposed by the forces induced from the heating current, such that the

electromagnetic forces at the regime around ±45 degrees latitude become weaker, while the electromagnetic forces near the equator developed. Correspondingly, the large recirculation loop in Figure 19 (a) which is dominated by positioning current starts to shrink, and another recirculation loop near the pole which is dominated by heating current grows. During this process, the convection velocity is reduced due to offset between the induced effects from positioning and heating current. In Figure 19 (c)-(h), the heating current increases from 10 A to 15 A, the positioner-dominated recirculation loop is overwhelmed by the heater-dominated recirculation loop gradually, and the convection velocity increases steadily. In Figure 19 (i), the positioner-dominated recirculation loop has disappeared, and the maximum electromagnetic forces appear near the equator. In Figure 19 (j)-(l), the convection flow starts to become turbulence when the heating current exceeds 30 A, and convection velocity almost linearly increases with the heating current, while the convection flows keep a similar pattern, as well as the distributions of electromagnetic body forces.

5 Discussion

5.1 Control Voltage vs. Current

In actual EML experiments, the positioner and heater are operated by a voltage controller. It is necessary to specify the relation between control voltage and coil current, which differs with different coil settings and facilities, so that the convection velocity inside levitated molten alloy droplet can be predicted with given voltage controller setting.

For SUPOS coils, the coil current and coil voltage has the following relations [23],

$$\begin{cases} I_0^H = \omega_H C_H U_0^H \\ I_0^P = \omega_P C_P U_0^P \end{cases} \tag{14}$$

And the coil voltage and control voltage has the following relations,

$$\begin{cases} U_0^H = 18.04 + 17.95 \cdot U_{ctr}^H \\ U_0^P = 12.03 + 12.03 \cdot U_{ctr}^P \end{cases} \tag{15}$$

Where $\omega_H = 2\pi \cdot 376$ kHz, $\omega_P = 2\pi \cdot 144$ kHz, $C_H = 448$ nF, $C_P = 2500$ nF; I_0^H and I_0^P stands for heating and positioning current in the coil, which is used in MHD simulation; U_0^H and U_0^P stands for heating and positioning voltage in the coil; U_{ctr}^H and U_{ctr}^P stands for EML control voltage for heater and positioner.

Combining equations (10) and (11), we have the following linear relation between coil current and control voltage, which is also plotted in Figure 20,

$$\begin{cases} I_0^H = 19.09 + 19.00 \cdot U_{ctr}^H \\ I_0^P = 27.21 + 27.21 \cdot U_{ctr}^P \end{cases} \tag{16}$$

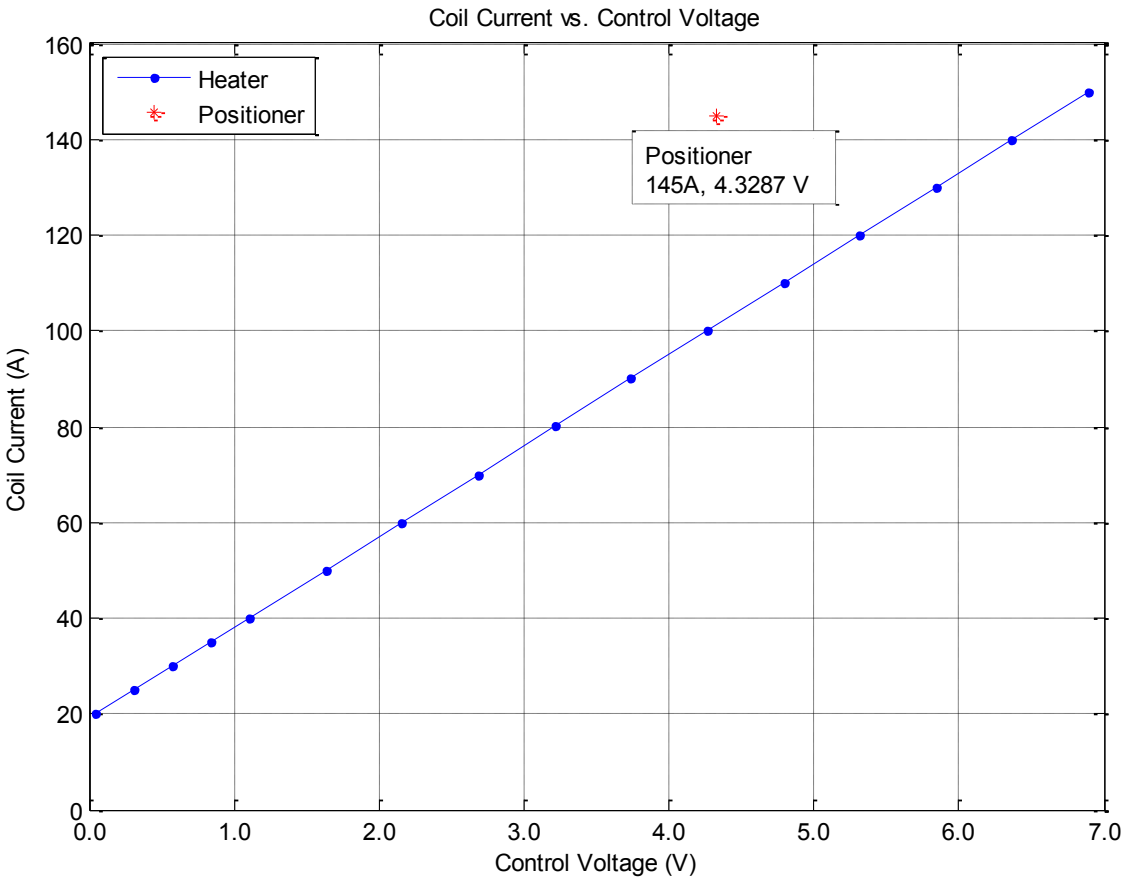

Figure 20: Coil Current vs. Control Voltage in SUPOS

In MHD simulation, the positioning current is fixed at 145 A which corresponds to control voltage of 4.3287 V in the positioner. With the heater off, the SUPOS coil still maintains a heating current near 20 A. The heating current will increases from 20 A to 150 A as the control voltage in the heater increases from 0 V to 6.8905 V.

The specific values of coil current versus control voltage are listed in Table 3.

Positioning Current (A)	Control Voltage of Positioner (V)
145A	4.3287V
Heating Current (A)	Control Voltage of Heater (V)
20	0.0477

25	0.3109
30	0.5741
35	0.8373
40	1.1005
50	1.6268
60	2.1532
70	2.6796
80	3.2059
90	3.7323
100	4.2587
110	4.7850
120	5.3114
130	5.8378
140	6.3641
150	6.8905

Table 3: Coil Current vs. Control Voltage in SUPOS

5.2 Equilibrium Temperatures

For one melt cycle in the EML experiment, the alloy sample will be melted and superheated from solidus to liquidus status with the heater on, and the molten sample will cool down to some undercooling degrees and recalesce to be solidified with the heater turned down. During the process, if the heater is set to a relatively higher control voltage, specifically, within the range from 3.6 V to 6.89V the molten sample may finally achieve an equilibrium temperature which is above its recalescence plateau. In this case, the molten sample will never achieve the testing temperature below the steady state temperature, and it may never recalesce with the heater setting.

It is necessary to evaluate the critical control voltage which allows the sample to recalescence for given undercooling degrees. MUSC simulator is utilized to generate Temperature-Time profiles with adjustable settings of control voltage, and investigate

the equilibrium temperature for each control voltage. The parameters used in MUSC simulator for $Fe_{50}Co_{50}$ sample is presented in Figure 21,

ID			CC_heat_s	0.00182	S
Mass	0.91886	g	CC_heat_l	0249509	S
Density Solid	8.4	g/cm^3	CC_off_l	0	W
Density Liquid	7.515	g/cm^3	CC_Pos_s	0.00016	S
Diameter	6.5	mm	CC_Pos_l	0022455	S
C_s	25.9	J/mol/K	CC_Off_s	0	W
C_l	41.1	J/mol/K	T solidus	1750	K
Heat	11500	J/mol	T liquidus	1755	K
Molm	57.4	g/mol	w0	0	g/cm^2 s^-1
Emiss	0.21		wT	0	K^-1

Figure 21: Parameters in MUSC Simulator

Figure 22 shows a normal process for one melt cycle in the EML experiment. The positioning control voltage (*Puste* in the figure) is set to be 4.3287 V during the whole melt cycle, recalescence plateau (orange dotted line) is assumed to be 1277 °C (200 degrees undercooling).

To melt and superheat the sample, heating control voltage is set to be 10.0 V (*Huste* in the figure), and the sample achieves about 2200 °C after about 50 seconds. Subsequently the heating control voltage is changed to 3.0 V, and the sample cools down to 1377 °C after another 20 seconds and recalesces.

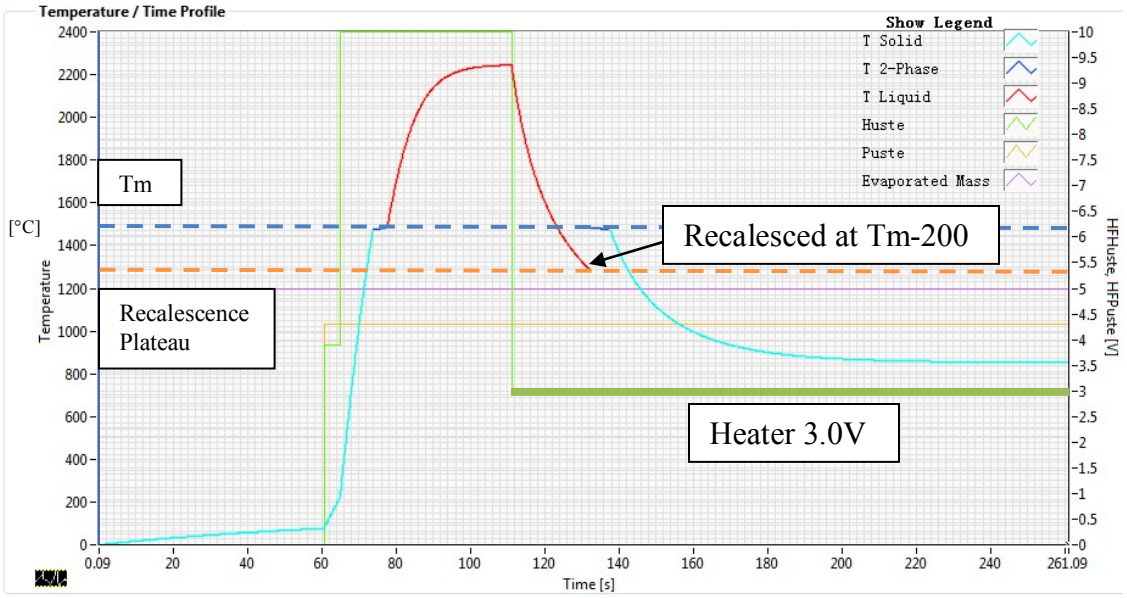

Figure 22: T-t Profile with 3.0 V Heating Control Voltages

Figure 23 shows an example with heating control voltage of 4.5 V that lead to an equilibrium temperature of 1302 °C (175 degrees undercooling), and the sample could not recalesce

Figure 24 shows another example with heating control voltage of 5.5 V that lead to an equilibrium temperature of 1502 °C (25 degrees superheating), the sample cools down even slower and could not recalesce either.

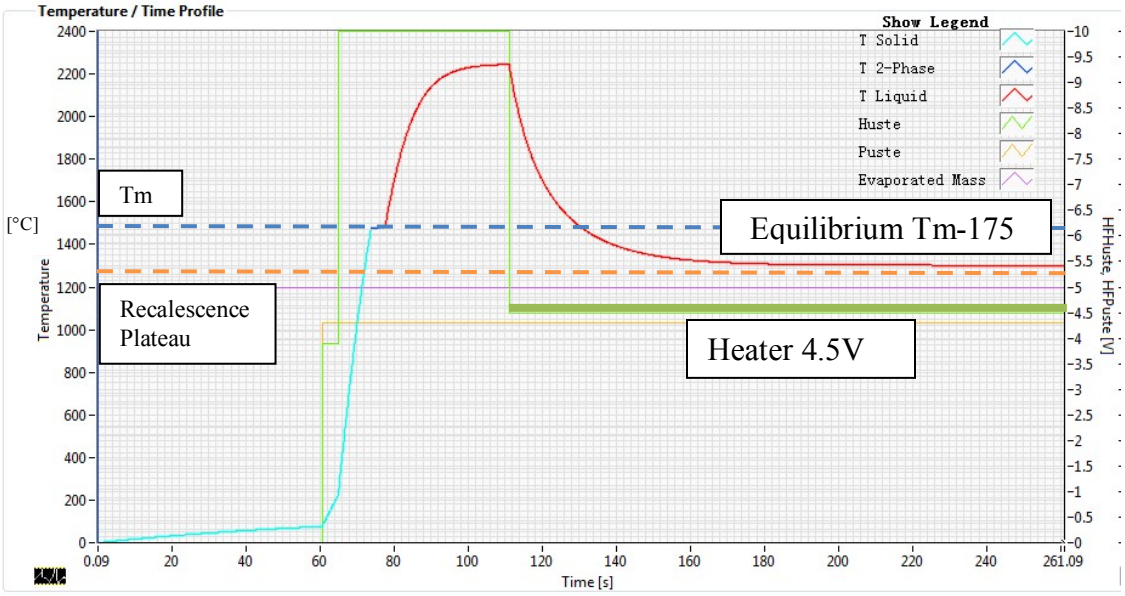

Figure 23: T-t Profile with 4.5 V Heating Control Voltages

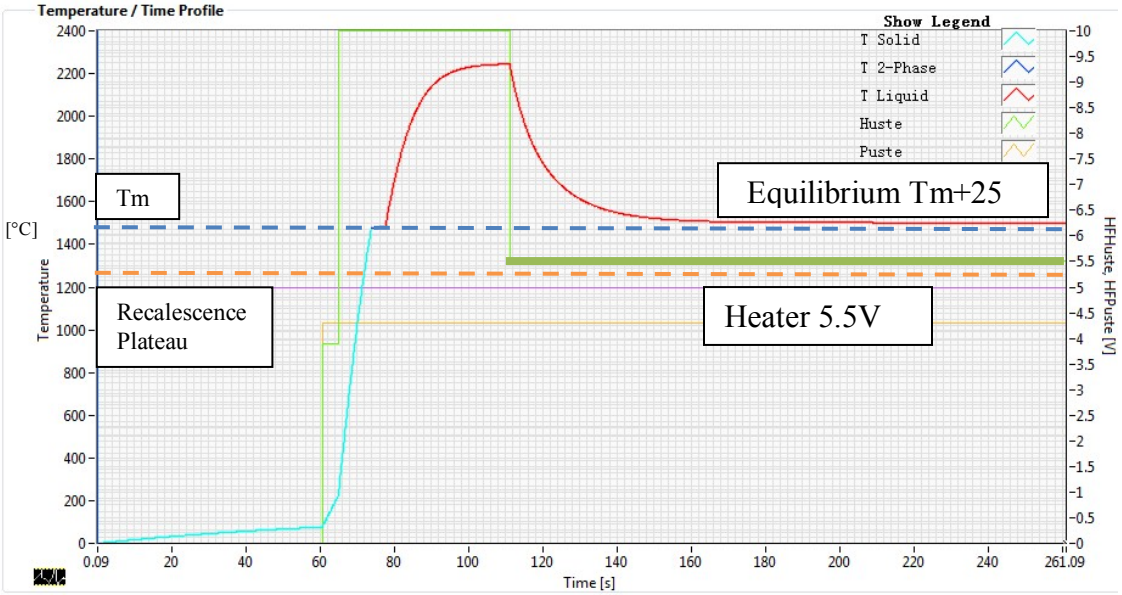

Figure 24: T-t Profile with 5.5 V Heating Control Voltages

Utilizing MUSC simulator, the equilibrium temperature is evaluated with heating control voltage changes from 0 V to 7.0 V, while the positioning control voltage is fixed at 4.3278 V. Figure 25 and Table 4 shows the equilibrium temperature changing with increased control voltages of heater.

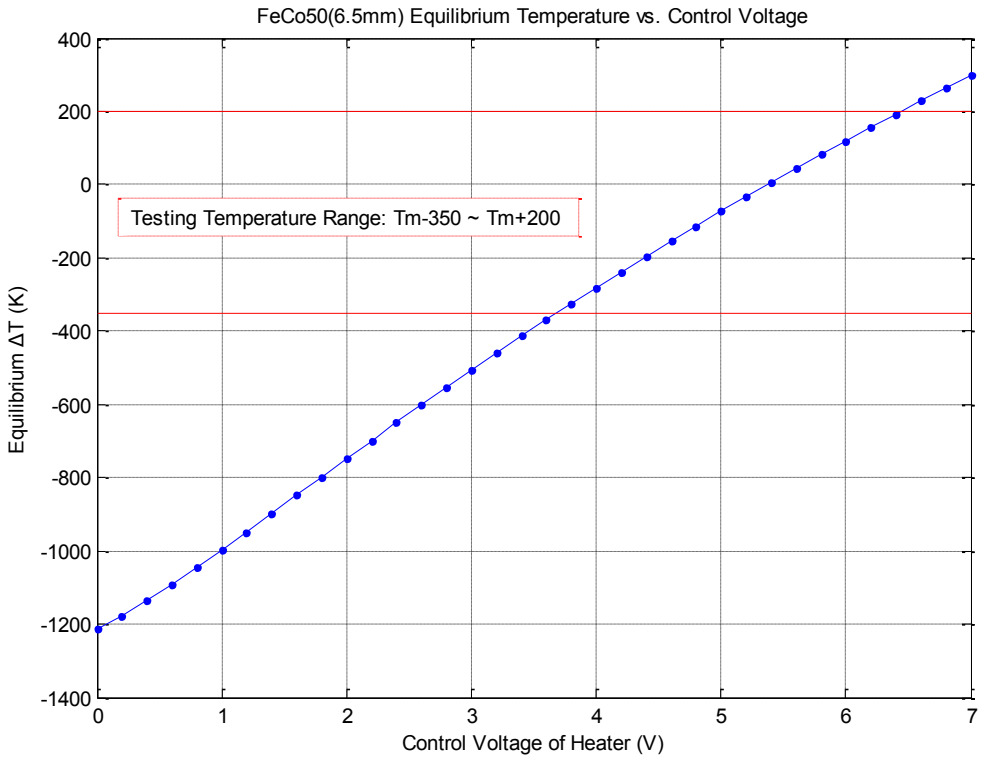

Figure 25: Equilibrium Temperature vs. Control Voltage of Heater

Control Voltage of Heater (V)	Equilibrium Temperature (K)	ΔT=Tm-T (K)
0.0	535.3	-1214.8
0.2	572.7	-1177.4
0.4	613.9	-1136.2
0.6	658.2	-1091.9
0.8	704.6	-1045.5
1.0	752.7	-997.4
1.2	801.8	-948.3
1.4	851.6	-898.5
1.6	901.7	-848.4
1.8	951.8	-798.3
2.0	1001.7	-748.4

2.2	1051.2	-698.9
2.4	1100.3	-649.8
2.6	1148.8	-601.3
2.8	1196.7	-553.4
3.0	1244.0	-506.1
3.2	1290.5	-459.6
3.4	1336.3	-413.8
3.6	1381.4	-368.7
3.8	1425.8	-324.3
4.0	1469.5	-280.6
4.2	1512.4	-237.7
4.4	1554.6	-195.5
4.5	1575.5	-174.6
4.6	1596.2	-153.9
4.7	1616.7	-133.4
4.8	1637.1	-113.0
4.9	1657.3	-92.8
5.0	1677.3	-72.8
5.1	1697.2	-52.8
5.2	1716.9	-33.2
5.3	1736.5	-13.6
5.4	1755.9	5.8
5.5	1775.2	25.2
5.6	1794.3	44.3
5.7	1813.3	63.3
5.8	1832.1	82.1
5.9	1850.8	100.8
6.0	1869.4	119.4
6.1	1887.8	137.8
6.2	1906.1	156.1
6.3	1924.3	174.3
6.4	1942.3	192.3
6.6	1978.0	228.0
6.8	2013.2	263.2
7.0	2047.9	297.9

Table 4: Equilibrium Temperature vs. Control Voltage

In EML experiment with SUPOS coils, for given undercooling degrees, critical control voltage is evaluated by linear interpolating the values presented in Table 4. The results are showed in Figure 26 and Table 5. To achieve the expected undercools, the control

voltage of heater should be less than the critical value unless the testing temperature would never achieve the desired given undercooling degrees. Thus, the red line in Figure 26 determines the upper limit of the control voltage. Additionally, we are interested in the double recalescence solidification process which requires undercooling larger than 50 K to achieve metastable BCC phase, so that the regime marked in red defined by both and upper limit of control voltage and the sample's ability to achieve metastable phase is accessible and also useful.

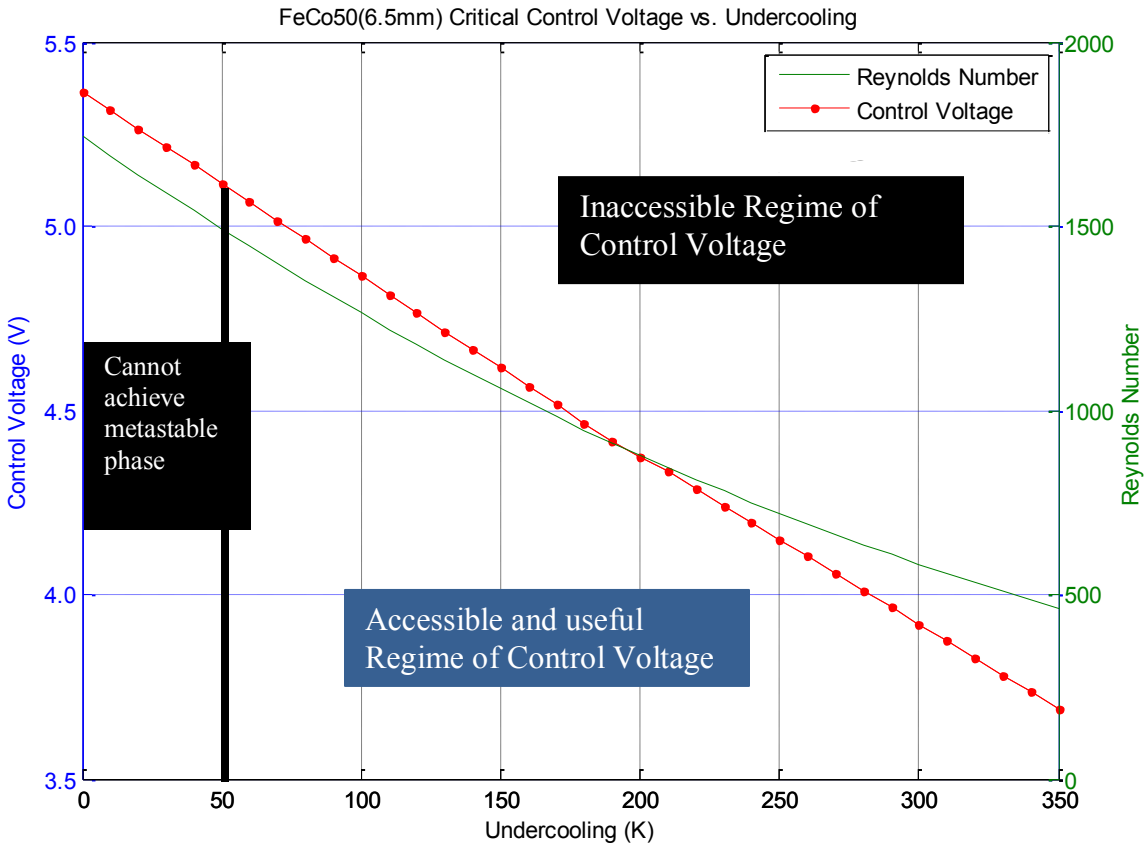

Figure 26: Critical Control Voltage vs. Undercooling

The positioning control voltage is fixed at 4.3278 V. With heating control voltage of 5.365 V, the equilibrium temperature archives the molten temperature; with heating control voltage below 3.6895 V, the equilibrium temperature will be below 1400 K

(undercooling 350 K), and the molten sample will always have chances to recalesce since mostly the recalesce plateau is above 350 K undercooling.

5.3 Limits to Convection Accessible

With selection of high heater control voltage settings in the EML, the test temperature would never fall below its an equilibrium temperature and the internal convection velocity of the molten sample will be limited, since the convection velocity is a function of the temperature. If the heater is set to a high value to achieve high stirring then the sample may not recalesce since it never achieves a low enough temperature to induce nucleation. Additionally, if the sample undercools only slightly, it will not undercool enough to access the metastable phase during recalescence either. Note that some convection must also result due to application of the positioned field to safely contain the sample within the test chamber.

Thus there are three competing limits. If a sample undercools deeply then the amount of convection that can be applied is limited by the sample equilibrium temperature but if the sample undercools too little then accessing the metastable phase is not possible. Application of the positioned field requires some amount of induce flow as well.

Thus, it is necessary to evaluate the critical convection velocity under different control voltage with given undercooling, so that the accessible range of the convection velocity will be predictable in support of space EML experiments. The critical convection velocity is showed in Table 5 and Figure 27.

Undercooling (K)	Temperature (K)	Critical Control Voltage of Heater (V)	Critical Convection Velocity (m/s)
0	1750	5.3651	0.2122
10	1740	5.3151	0.2095
20	1730	5.2651	0.2067
30	1720	5.2151	0.2040
40	1710	5.1651	0.2013
50	1700	5.1151	0.1986
60	1690	5.0651	0.1959
70	1680	5.0151	0.1931
80	1670	4.9651	0.1904
90	1660	4.9151	0.1877
100	1650	4.8651	0.1850
110	1640	4.8151	0.1822
120	1630	4.7651	0.1796
130	1620	4.7151	0.1769
140	1610	4.6651	0.1742
150	1600	4.6151	0.1715
160	1590	4.5651	0.1689
170	1580	4.5151	0.1662
180	1570	4.4651	0.1635
190	1560	4.4151	0.1609
200	1550	4.3743	0.1585
210	1540	4.3335	0.1562
220	1530	4.2875	0.1537
230	1520	4.2415	0.1513
240	1510	4.1955	0.1488
250	1500	4.1495	0.1464
260	1490	4.1035	0.1440
270	1480	4.0575	0.1415
280	1470	4.0115	0.1391
290	1460	3.9655	0.1366
300	1450	3.9195	0.1341
310	1440	3.8735	0.1317
320	1430	3.8275	0.1293
330	1420	3.7815	0.1268
340	1410	3.7355	0.1244
350	1400	3.6895	0.1220

Table 5: Critical Control Voltage and Convection Velocity vs. Undercooling

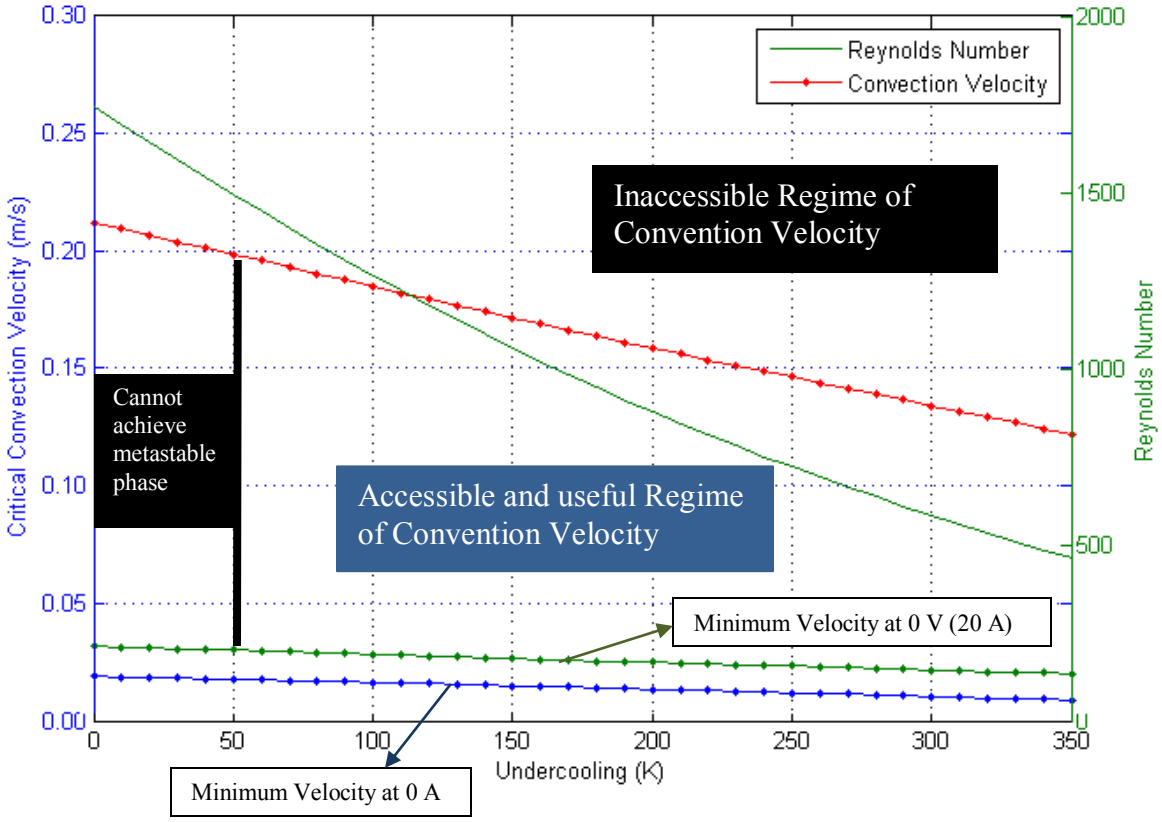

Figure 27: Critical Convection Velocity and Re vs. Undercooling

In the experiment, when the molten sample achieves certain equilibrium undercools, if control voltage is turned down, the sample's temperature will decrease correspondingly, and achieve its recalescence plateau then start the solidification process. During this process, the internal convection flow will drop below the critical velocity. Thus, the red line in Figure 27 defines the upper limit of the internal convection velocity, and the corresponding Reynolds numbers are showed as the green line. Additionally, there is minimum velocity as the lower limit that is defined by the lower green and blue line. Since the EML will maintain some minimum coil current of heater around 20 A while the control voltage is 0 V, and there is positioning current exist while the heating current is 0 A, there are two lower limits to the internal convection velocity.

Furthermore, if the sample undercools more than 300 degrees it will always be laminar and thus not useful. If a sample undercools around 150 it will be able to achieve a maximum Reynolds number of around 1000 at a control voltage of about 4.5 V and a velocity of around 0.15 m/s. If a sample undercools less than the critical undercooling of 50 degrees, then we can't access the double recalescence and the sample is not useful.

5.4 Accessible Convection Velocity vs. Control Voltage

The convection velocity with limitations inside molten $Fe_{50}Co_{50}$ droplet is calculated as function of testing temperature and the control voltage in EML, converting the results in section 4.2 from coil current to control voltage. Figure 28 and Figure 29 shows the accessible convection velocity versus the control voltage and testing temperature. The positioning control voltage is fixed at 4.3278 V, the heating control voltage increases from 0.048 V to 5.838 V. With the undercooling regime, the internal convection of levitated molten $Fe_{50}Co_{50}$ droplet is predictable and can be used to conduct further research on solidification process. With both of the superheating and undercooling regime, the predication would support the measurement of molten sample's thermophysical properties.

The black line in Figure 28 shows the undercool limitations. Beyond this limitation, the sample cannot achieve further undercools with the corresponding control voltage. And there is also positioner limitation that the control voltage of the positioner will maintain a minimum convection velocity inside the molten sample. All the results show what the possible internal convection velocity will be under certain control voltage, and at what

control voltage the convection flow will be laminar or turbulent by evaluating the Reynolds number. The laminar flow is primarily dominated by viscous effect, and the viscous effect is much less than inertial effect in turbulence. Specially, the flow can be assumed to be super laminar while the Reynolds number exceed the laminar-turbulent transition point, such that the viscous effect is still influence the flow but it becomes unstable simultaneously, and turn out to be turbulent gradually. With an extremely high Reynolds number, the flow might be developed to fully turbulence with highly irregularity. It should be noticed that in the present case, the actual fully turbulence might not be developed since the eddies inside the flow are the same order of magnitude of the sample size.

With fixed control voltage, the convection velocity inside the molten sample will decrease as the temperature cools down, until the molten sample reaches its recalescence temperature or undercool limits. Additionally, if the molten sample temporarily stays at a certain temperature, and the control voltage is turn down, the temperature of the sample will decrease as well as the convection velocity. In the laminar case, the solid lines show the laminar flow with Re smaller than 525, and dash lines show the super laminar flow with Re slightly larger than 525, the flow is completely laminar and in the transition process between laminar and turbulent flow. In the turbulent case, the solid isothermal lines show the convection velocity with a corresponding Reynolds number larger than 525, and the flow is expected to be turbulent; for the dash lines, the corresponding Reynolds number is within 300 to 525, the flow is not turbulent, but the turbulence is in the developing process. The results

showed in Figure 28 can provide predictions of the internal convection velocity based on the testing temperature and power settings in experiments. For example, sample undercools to 200 K and has 0.17 m/s flow velocity, with 4.5 V voltages.

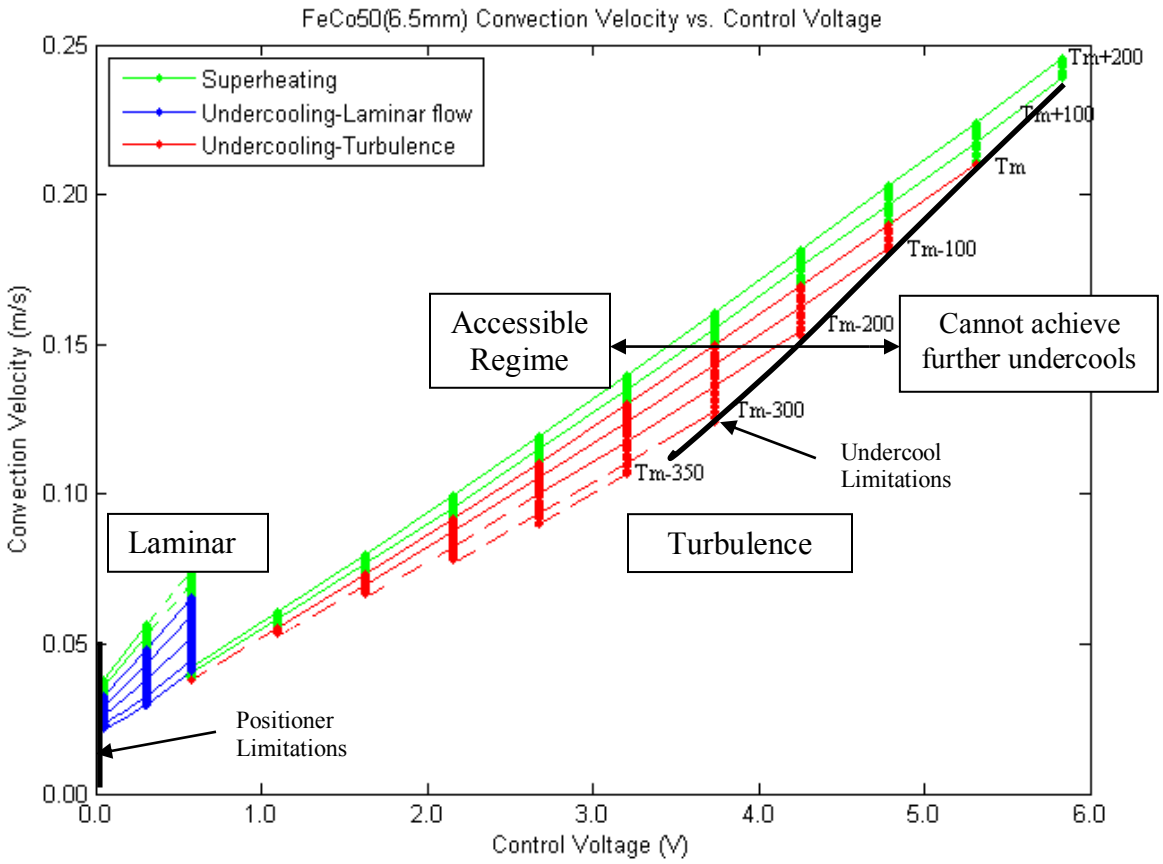

Figure 28: $Fe_{50}Co_{50}$ Droplet Accessible Convection Velocity vs. Control Voltage

Figure 29 shows the predicted internal convection velocity versus temperature and control voltage in three dimensions, with laminar and turbulent model respectively. Providing the temperature-time and control voltage-time profile, a corresponding convection velocity changing path can be found on the plot.

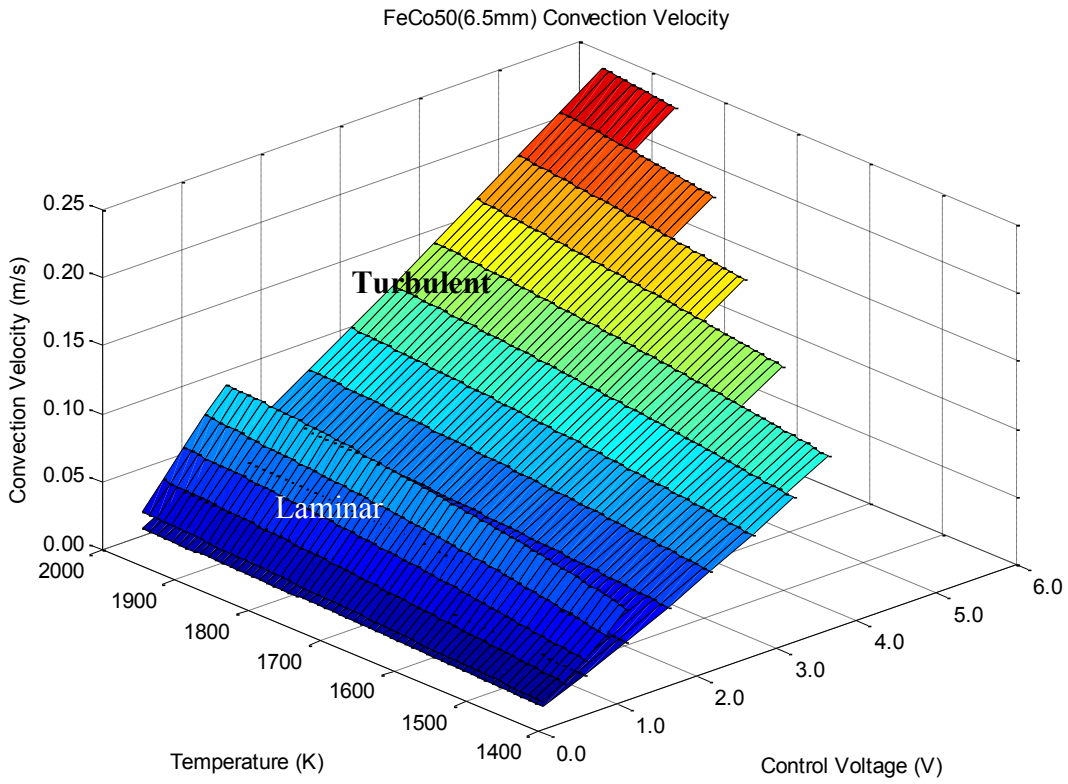

Figure 29: $Fe_{50}Co_{50}$ Droplet Accessible Convection Velocity (3D)

Reynolds number is calculated to characterize the internal convection flow. With limits to convection accessible, there is corresponding limitations on Reynolds number. Figure 30 shows the accessible Reynolds number characterizing the convection flow inside levitated $Fe_{50}Co_{50}$ droplet. As descried in chapter 4.1, the internal convection velocity and the Reynolds number of the molten droplet is unknown in an actual experiment, and it is estimated that laminar-turbulent transition regime is of Reynolds number around 300 to 700, centered at 525. There is an overlap area between the laminar and turbulent model since the laminar-turbulent transition occurs in this range, and the exact transition point is unknown in experiment. The dash lines in Figure 30 show the extended computation results of the laminar and turbulent model, and these

results provide an overall prediction of the laminar-turbulent transition behavior for actual experiments.

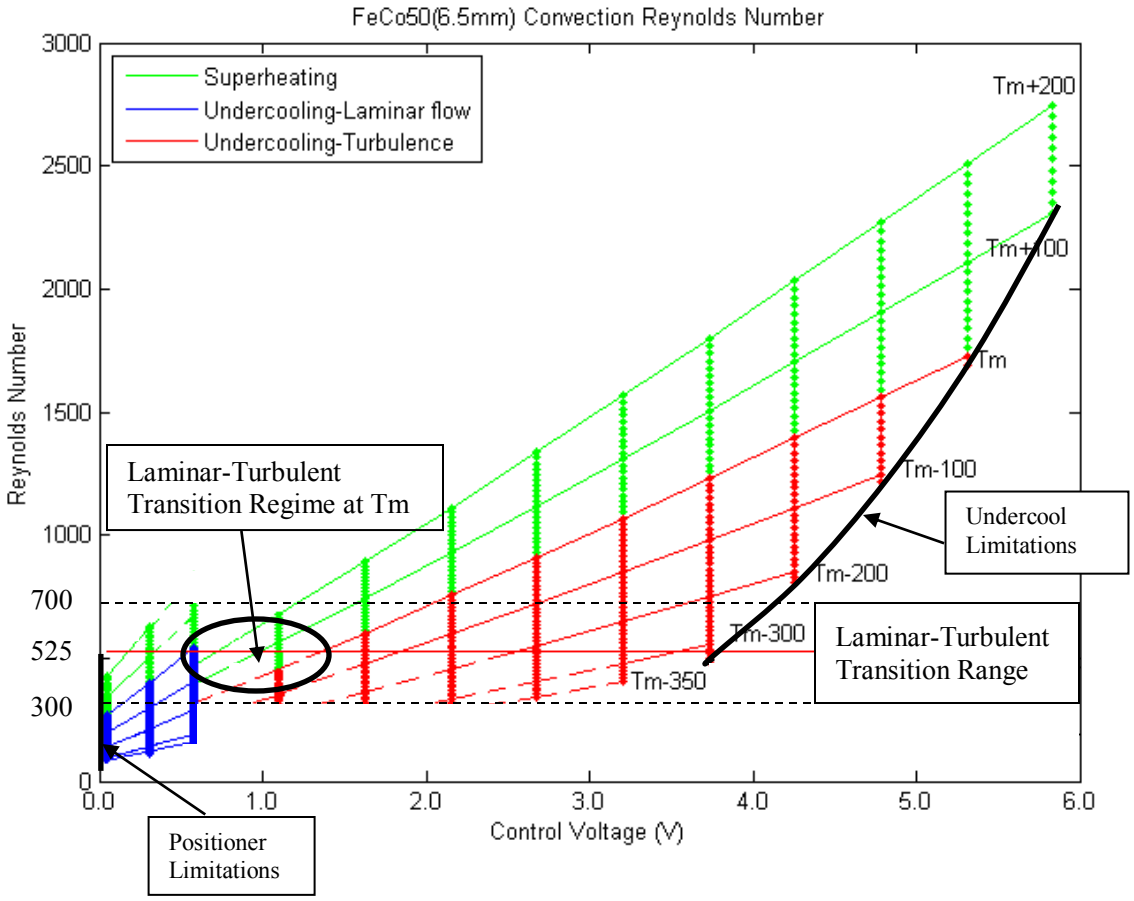

Figure 30: $Fe_{50}Co_{50}$ Droplet Accessible Reynolds Number vs. Control Voltage

At the molten temperature of $Fe_{50}Co_{50}$ (Tm=1750 K), the convection flow stays laminar with heating current from 0 V to 0.3109 V, and starts to show some turbulence at 0.5741 V, afterwards it becomes completely turbulence from around 1.5 V. For deep undercooling such as Tm-300 (1450 K), the convection flow becomes turbulent while the heating control voltage is around 3.5 V. In general, the laminar-turbulence transition occurs at the heating control voltage around 0.5 V to 3.0 V depending on the testing temperature, normally from Tm+150 to Tm-200.

6 Conclusions

MHD Modeling

- A magnetohydrodynamic (MHD) model simulating the internal convection of electromagnetically levitated droplets is developed using ANSYS-Fluent;
- The MHD model is applied to levitated $Fe_{50}Co_{50}$ droplet within SUPOS coils, and the internal convection velocity of the droplet is predicted as function of coil current and testing temperature.

Convection Accessible in EML

- Equilibrium temperature is evaluated using MUSC simulator with adjustable EML control voltage which can be converted from the coil current;
- For given undercooling, critical control voltage and convection velocity is calculated which defines the accessible range of internal convection flow; Accessible internal convection velocity of levitated $Fe_{50}Co_{50}$ droplet is evaluated as function of control voltage and testing temperature
- Corresponding accessible Reynolds number is calculated to characterize the convection flow, and the laminar-turbulent transition regime is found to be at heating control voltage of 0.5 V to 3.0 V with fixed positioning control voltage of 4.3278 V, for undercooling temperatures between 0 K and 300 K.

7 Future Work

More composition of Iron-Cobalt alloy system should be studied, such as $Fe_{60}Co_{40}$ and $Fe_{70}Co_{30}$, as well as other alloy systems such as steels. With the predicted convection velocity inside the electromagnetically levitated molten alloys, further research on the solidification process could be conducted, comparing the effects of different composition for certain alloy systems.

Precise measurement of thermophysical properties could be performed utilizing ground based ESL or microgravity EML facilities, to provide reliable density and viscosity values of molten alloys, in both of the superheated and undercooled regime.

8 References

[1] D.M. Matson, D.J. Fair, R.W. Hyers, and J.R. Rogers, "Contrasting Electrostatic and Electromagnetic Levitation Experimental Results for Transformation Kinetics of Steel Alloys," Annals of the New York Academy of Sciences,1027, (2004), pp. 435–446.

[2] A.B. Hanlon, D.M. Matson, and R.W. Hyers, "Internal convective effects on the lifetime of the metastable phase in under cooled Fe-Cr-Ni alloys", Philosophy Magazine Letter, 86, (2006), pp. 165–174.

[3] R.W. Hyers, D.M. Matson, K.F. Kelton, J.R. Rogers, "Convection in Containerless Processing", Annals of the New York Academy of Sciences, 1027, (2004), pp. 474–494.

[4] M.C. Flemings, D.M. Matson, J.R. Rogers, et al., "Levitation observation of dendritic evolution in steel ternary alloy rapid solidification (LODESTARS) ", NASA Science Requirements Document LODESTARS-RQMT-001, (2003).

[5] A.B. Hanlon, D.M. Matson, and R.W. Hyers, "Microgravity Experiments on the effect of Internal Flow on Solidification of Fe-Cr-Ni Stainless Steels", Annals of the New York Academy of Sciences,1077, (2006), pp. 33–48.

[6] D.A. Porter and K.E. Easterling, "Phase Transformations in Metals and Alloys", Nelson Thornes, Cheltenham, Gloucestershire, (2001), pp. 514.

[7] R.W Hyers, G. Trapaga and A.B. Hanlon, "Laminar-turbulent transition in an electromagnetically levitated droplet Metal", Metallurgical and Materials Transactions B, 34B, (2003), pp. 29–36.

[8] R.W. Hyers, "Modeling and Experiments on Electromagnetic Levitation for Material Processing", Ph.D. Thesis, Massachusetts Institute of Technology, 1998.

[9] N. El-Kaddah and J. Szekely, "The Electromagnetic Force Field, Fluid Flow Field, and Temperature Profiles in Levitated Metal Droplets", Metallurgical Transactions B, 14(3), (1983), pp. 401-410.

[10] J.H. Zong, B.Q. Li, J. Szekely, "The Electrodynamic and Hydrodynamic Phenomena in Magnetically-levitated Droplets- II. Transient Behavior and Heat Transfer Considerations", Acta Astronautica, 29(4), (1992), pp. 305-311.

[11] B.Q. Li, " The Transient Magnetohydrodynamic Phenomena in Electromagnetic Levitation Process", International Journal of Engineering Science, 32 (8), (1994). pp. 1315-1336.

[12] R.W. Hyers, "Fluid flow effects in levitated droplets", Measurement Science and Technology, 16, (2005), pp. 394–401.

[13] J. Lee, X. Xiao, D.M. Matson, and R.W. Hyers, "Characterization of Fluid Flow inside Electromagnetically-Levitated Molten Iron-Cobalt Droplets for ISS Experiments", TMS, 2013.

[14] G. Lohoefer and J. Pillar, "The New ISS Electromagnetic Levitation Facility: MSL-EML", The 40th AIAA Aerospace Sciences Meeting and Exhibit, Reno NV, January 2002.

[15] Y. Kita and Z. Morita, "The Electrical Resistivity of Liquid Fe-Ni, Fe-Co, and Ni-Co Alloys", Journal of Non-Crystalline Solids, 61&62, (1984), pp. 1079-1084.

[16] S. Watanabe, "Densities and Viscosities of Iron, Cobalt and Fe-Co Alloy in Liquid State", Transactions of the Japan Institute of Metals, 12, (1971), pp. 17-22.

[17] S. Sato, K. Sugisawa, D. Aoki, and T. Yamamura, "Viscosities of Fe-Ni, Fe-Co, and Ni-Co Binary Metals", Measurement Science and Technology, 16, (2005), pp. 363-371.

[18] S. Berry, R.R. Hyers, B. Abedian and L.M. Racz, "Modeling of turbulent flow in electromagnetically levitated metal droplets", Metallurgical and Materials Transactions B, 31B, pp. 171–178.

[19] S. Binder, "Undercooling and solidification of tetragonal Ni2B under different convective flow conditions", Ph.D. Dissertation, Ruhr University Bochum, 2010.

[20] J. Lee, D.M. Matson, S. Binder, M. Kolbe, D. Herlach, and R.W. Hyers, "Magnetohydrodynamic Modeling and Experimental Validation of Convection inside an Electromagnetically-Levitated Co-Cu Droplet", in submission, (2013).

[21] G. Lohöfer, German Aerospace Center (DLR), personal communication, (2013).

[22] J. Rodriguez and D.M. Matson , unpublished results (2013).

[23] J. Brillo, I. Egry, and T. Matsushita, "Density and excess volumes of liquid copper, cobalt, iron and their binary and ternary alloys", International Journal of Materials Research, 97, (2006), pp.1526-1532.

[24] T. Nishi, H. Shibata, Y. Waseda, and Hiromichi Ohta, "Thermal conductivities of molten iron, cobalt, and nickel by laser flash method", Metallurgical and Materials Transactions A, 34(12), (2003), pp. 2801-2807.

[25] T. Iida, and R. Guthrie, "The physical properties of liquid metals", Clarendon Press, (1988).

[26] ANSYS-Fluent 12.0 User's Guide, ANSYS, Inc.

Appendices

User defined function (UDF) for ANSYS-Fluent:

"f_bdy.udf.c"

```
#include "udf.h"
#define SIZE 400
#define RADNUM 20
#define ANGNUM 20

DEFINE_SOURCE(f_bdy,c,t,dS,eqn)
{
int i, j, m, n;
float x[SIZE+2*RADNUM], y[SIZE+2*RADNUM], fx[SIZE+2*RADNUM], fy[SIZE+2*RADNUM],
r[SIZE+2*RADNUM], theta[SIZE+2*RADNUM];
float radial[RADNUM], angular[ANGNUM];
float mx, my, mrad, mang, mfx, mfy, mx1, my1, mfx1 ,mfy1;

float mtheta, mr, theta1, r1, theta3, r2, fx1, fy1, fx2, fy2, fx3, fy3, fx4, fy4, fxa, fya,
fxb, fyb;
int num1[SIZE+2*RADNUM], num2[SIZE+2*RADNUM], num3[SIZE+2*RADNUM];
int indexmrad, indexmang;

/* 1.Read EMF data */
/* 2.Add two additional radial points with negative x values */
for(i=0; i<RADNUM; i++)
{
x[i] = -x[i+RADNUM];
y[i] = y[i+RADNUM];
x[i+RADNUM+SIZE] = -x[i+SIZE];
y[i+RADNUM+SIZE] = y[i+SIZE];
fx[i] = -fx[i+RADNUM];
fy[i] = fy[i+RADNUM];
fx[i+RADNUM+SIZE] = -fx[i+SIZE];
fy[i+RADNUM+SIZE] = fy[i+SIZE];
num1[i+SIZE] = num1[i+SIZE-1] + 1;
num1[i+RADNUM+SIZE] = num1[i+SIZE-1] + RADNUM + 1;
num2[i+SIZE] = num2[i];
num2[i+RADNUM+SIZE] = num2[i];
num3[i+SIZE] = num3[i] + RADNUM;
num3[i+RADNUM+SIZE] = num3[i] + RADNUM + 1;
}

/* 3.Calculate radial distance of grid points (mags) on a radial line */
for(i=0; i<RADNUM; i++)
{
radial[i] = sqrt(pow(x[i], 2)+pow(y[i], 2));
}

/* 4.Calculate angles of radial lines */
for(i=0; i<ANGNUM; i++)
{
```

```
angular[i] = atan(y[2*RADNUM-1+ANGNUM*i]/x[2*RADNUM-1+ANGNUM*i]);
}

C_CENTROID(xx,c,t);

/* 5.Calculate angle and radial distance of mesh points (fluent) */

mx1=xx[0];
my1=xx[1];

mx=my1;
my=mx1;

mang = atan(my/mx);

if(sqrt(pow(mx, 2)+pow(my, 2)) >= radial[RADNUM-1])
{
mrad = radial[RADNUM-1];
}
else
{
mrad = sqrt(pow(mx, 2)+pow(my, 2));
}

/* 6.Determine which mags grid region the fluent node falls onto */
if(mrad < radial[0])
{
indexmrad = 0;
}

else
{
j = 0;
while(mrad > radial[j])
{
indexmrad = j+1;
j = j + 1;
}
}


if(mang > angular[0])
{
indexmang = 0;
}

else if(mang < angular[ANGNUM-1])
{
indexmang = ANGNUM;
}
else
{
j = 0;
while(mang <= angular[j])
{
```

```
indexmang = j+1;
j = j + 1;
}
}

/* 7.Interpolation */
mtheta = mang;
mr = mrad;

m = indexmrad;
n = indexmang;

r1 = radial[m-1];
r2 = radial[m];
theta1 = angular[n-1];
theta3 = angular[n];

fx1 = fx[m-1+RADNUM*n];
fy1 = fy[m-1+RADNUM*n];
fx2 = fx[m+RADNUM*n];
fy2 = fy[m+RADNUM*n];
fx3 = fx[m-1+RADNUM*(n+1)];
fy3 = fy[m-1+RADNUM*(n+1)];
fx4 = fx[m+RADNUM*(n+1)];
fy4 = fy[m+RADNUM*(n+1)];


fya = ((theta1-mtheta)*fy3+(mtheta-theta3)*fy1)/(theta1-theta3);
fyb = ((theta1-mtheta)*fy4+(mtheta-theta3)*fy2)/(theta1-theta3);

mfy = ((r2-mr)*fya+(mr-r1)*fyb)/(r2-r1);
mfx1=mfy;

return mfx1;
}
```